Ore Geology Reviews 63 (2014) 444–464

Contents lists available at ScienceDirect

Ore Geology Reviews

journal homepage: www.elsevier.com/locate/oregeorev

Reprint of "Depositional environment and tectonic implications of the Paleoproterozoic BIF in Changyi area, eastern North China Craton: Evidence from geochronology and geochemistry of the metamorphic wallrocks"

Ting-Guang Lan [a,b,*], Hong-Rui Fan [a], Fang-Fang Hu [a], Kui-Feng Yang [a], Ya-Chun Cai [a], Yong-Sheng Liu [c]

[a] Key Laboratory of Mineral Resources, Institute of Geology and Geophysics, Chinese Academy of Sciences, Beijing 100029, China
[b] State Key Laboratory of Ore Deposit Geochemistry, Institute of Geochemistry, Chinese Academy of Sciences, Guiyang 550002, China
[c] State Key Laboratory of Geological Processes and Mineral Resources, China University of Geosciences, Wuhan 430074, China

ARTICLE INFO

Article history:
Received 25 June 2013
Received in revised form 20 October 2013
Accepted 23 January 2014
Available online 9 June 2014

Keywords:
Banded iron formation
Metamorphic wallrock
Protolith
Paleoproterozoic
Continental rift
North China Craton

ABSTRACT

The Changyi banded iron formation (BIF) in the eastern North China Craton (NCC) occurs within the Paleoproterozoic Fenzishan Group. Three types of metamorphic wallrocks interbedded with the BIF bands are identified, including plagioclase gneisses and leptynites, garnet-bearing gneisses and amphibolites. Protolith reconstruction suggests that the protoliths of the plagioclase gneisses and leptynites are mainly graywackes with minor contribution of pelitic materials, the garnet-bearing gneisses are Fe-rich pelites contaminated by clastics, and the amphibolites are tholeiitic rocks. Trace elements of La, Th, Sc and Zr of the plagioclase gneisses and leptynites and the garnet-bearing gneisses support that these meta-sedimentary rocks were probably derived from recycling of Archean rocks with felsic and mafic materials differentiated into different rock types. $^{207}Pb/^{206}Pb$ ages of detrital zircons from the meta-sedimentary rocks concentrate at 2.7–3.0 Ga, confirming their derivation from the Archean rocks. The presence of several Paleoproterozoic detrital zircons (2240 to 2246 Ma), however, also suggests minor involvement of Paleoproterozoic materials. The Archean detrital zircons have $\varepsilon_{Hf}(t)$ values varying from −0.7 to 7.6, which mainly fall between the 3.0 Ga and 3.3 Ga average crustal evolution lines on the age vs. $\varepsilon_{Hf}(t)$ diagram, further illustrating that the rocks providing materials for the meta-sedimentary rocks mainly originated from partial melting of a Mesoarchean crust. This is strongly supported by their crust-like trace element distribution patterns (such as Nb, Ta, P and Ti depletion) and ancient Nd depleted mantle model ages (T_{DM} = 2.9–3.4 Ga). In addition, the remarkably high $\varepsilon_{Hf}(t)$ values (7.5 to 9.3) of the Paleoproterozoic detrital zircons constrain the Paleoproterozoic materials to originate from a depleted mantle. The amphibolites show low SiO_2 (46.5 to 52.8 wt.%) and high MgO (5.68 to 10.9 wt.%) contents, crust-like trace element features and low $\varepsilon_{Nd}(t)$ values (−4.5 to −0.3), suggesting that these ortho-metamorphic rocks were mainly derived from subcontinental lithospheric mantle with some contamination by Archean crustal materials. Since an intra-continental environment was required for the formation of the above metamorphic rocks, these rocks not only confine the depositional environment of the Changyi BIF to be an intra-continental rift, but also support the rifting processes of the eastern NCC during Paleoproterozoic.

1. Introduction

As the unique product in Precambrian, the deposition of iron formation (IF) not only relates to the evolution of life, ocean and atmosphere, but also to the origin and growth of continents (Trendall, 2002). Since depositional environment is vital in controlling the lithological and mineralogical features of IF, Gross (1980) proposed a popular classification of IF into Lake Superior-type and Algoma-type. Gross (1983) considered that the Lake Superior-type hosted in clastic and carbonate sediments without obvious volcanic associations commonly developed along the margins of cratons or continental platforms, whereas the Algoma-type typically associated with volcanic rocks and graywackes occurred under more dynamic tectonic conditions, possibly comparable to present day spreading ridges on the ocean floor. However, Trendall (2002) regarded that the above classification tends to break down if a global view was taken and thus a division of IF into BIF (banded iron formation) and GIF (granular iron formation) was recommended based on lithological criteria. The principal features of GIF that differentiate it

DOI of original article: http://dx.doi.org/10.1016/j.oregeorev.2014.01.007.
* Corresponding author at: Key Laboratory of Mineral Resources, Institute of Geology and Geophysics, Chinese Academy of Sciences, Beijing 100029, China. Tel.: +86 851 5603298.
E-mail address: lantingguang@126.com (T.-G. Lan).

0169-1368/$ – see front matter © 2014 Elsevier B.V. All rights reserved.
http://dx.doi.org/10.1016/j.oregeorev.2014.06.003

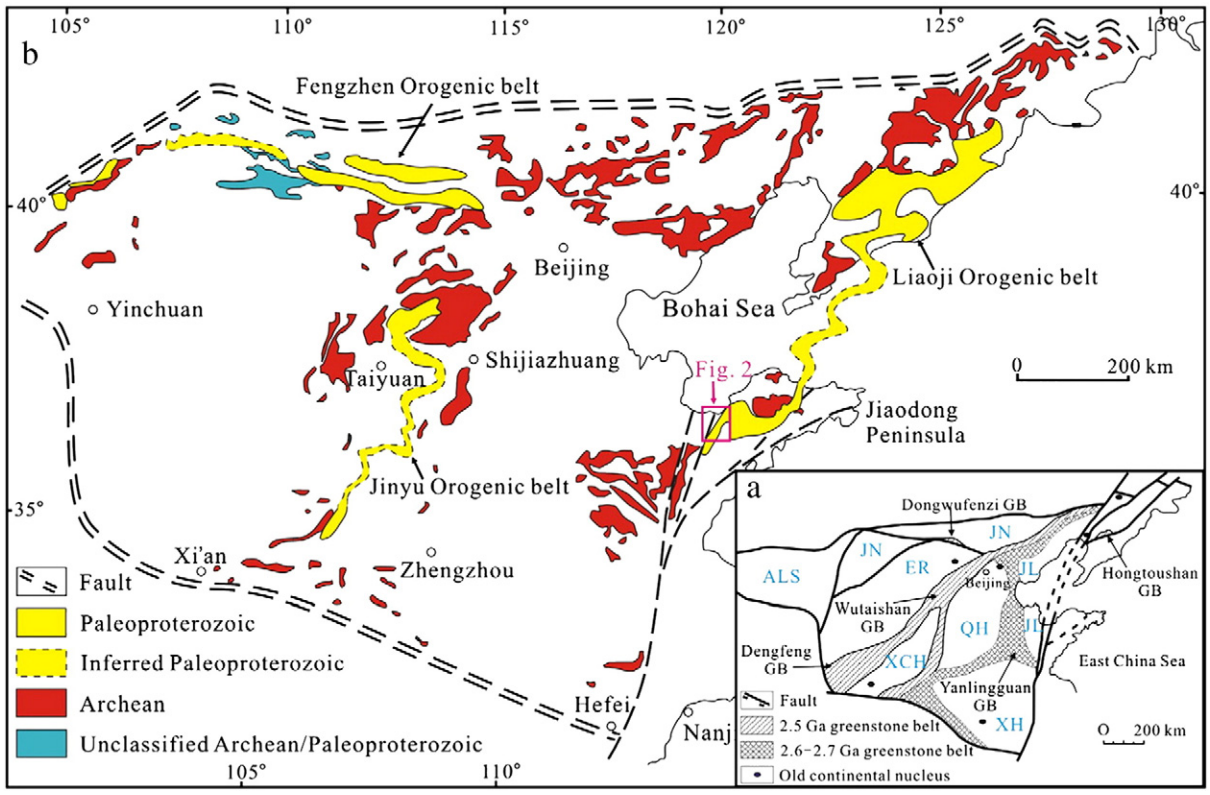

Fig. 1. (a) Sketch map of the NCC showing distribution of ancient nuclei, Archean micro-blocks and greenstone belts. (b) Distribution of Palcoproterozoic mobile belts of the North China Craton. Both (a) and (b) are modified after Zhai and Santosh (2011). JL: Jiaoliao Block; QH: Qianhuai Block; OR: Ordos Block; JN: Jining Block; XCH: Xuchang Block; XH: Xuhuai Block; ALS: Alashan Block; GB: greenstone belt.

from BIF are the granular, sandstone-like texture, the presence of current-generated structures and coarser banding, which suggest a shallow-water, high-energy environment (Trendall, 2002). No matter which division is more reasonable, both of them suggest that the IFs could occur in different depositional environments and the depositional background could be reconstructed according to their lithological associations.

BIFs have been widely found in the North China Craton (NCC), which are mostly Archean Algoma-type (Shen et al., 2005; Wan et al., 2012; Zhang et al., 2012a). Paleoproterozoic BIFs were only sporadically found with small scale in restricted areas. This distribution feature strongly contrasts with that of the BIFs around the world. Based on the statistics from Huston and Logan (2004), it is concluded that the Archean Algoma-type BIFs only occupy the majority in number, whereas the Paleoproterozoic Lake Superior-type BIFs constitute the vast abundance. The scarcity of Paleoproterozoic BIFs in the NCC, therefore, suggests that the NCC may have experienced a particular Paleoproterozoic evolutional history.

The Changyi BIF, located at the eastern NCC and mainly associated with metamorphic wallrocks of plagioclase gneisses and leptynites, garnet-bearing gneisses and amphibolites, was produced during Paleoproterozoic (2193–2240 Ma, Lan et al., 2013). As one of the rare Paleoproterozoic BIFs in the NCC, the Changyi BIF provides an important key to reveal the origin of the Paleoproterozoic BIFs and the Paleoproterozoic geological evolution of the eastern NCC. Therefore, in this paper, we report petrological, geochronological and geochemical data of the wallrocks of the Changyi BIF with a view to constrain the depositional environment of the Paleoproterozoic BIF and further to evaluate the Paleoproterozoic tectonic background of the eastern NCC.

2. Regional geology

Covering an area of about 1,500,000 km^2 and containing Archean cores of 2.5–3.8 Ga, the North China Craton (NCC) is the largest and oldest craton in China (Zhao et al., 2001). The craton is mainly composed of basements of Archean to Paleoproterozoic tonalite–trondhjemite–granodiorite (TTG) gneisses and greenschist to granulite facies volcano-sedimentary rocks (Zhao et al., 2001) covered by Paleo-Mesoproterozoic to Ordovician volcano-sedimentary rocks, Carboniferous to Permian terrestrial clastic rocks, and Mesozoic basin deposits. It has been widely accepted that the NCC formed by amalgamation of a number of micro-continental blocks (Zhai and Santosh, 2011; Zhao et al., 2012). However, the number of constituent blocks, and when and how they were assembled to form the coherent basement of the craton remain unresolved, resulting in a variety of models for the tectonic subdivision and amalgamation of the craton (Zhao et al., 2012, and references therein). At least two main models have been hotly debated in recent years. One considers that at least seven Archean micro-blocks (include the Jiaoliao, Qianhuai, Ordos, Jining, Xuchang, Xuhuai and Alashan blocks) built the basic tectonic architecture of the NCC at ca. 2.5 Ga through amalgamation (cratonization), and subsequently the NCC experienced an orogenic cycle from rifting to subduction–collision along three major Paleoproterozoic orogenic belts (termed the Fengzhen, Liaoji and Jinyu Orogenic belts) during 2350–1970 Ma with following regional high-grade metamorphism at 1950–1820 Ma (Zhai and Santosh, 2011, and references therein). The other model is remarkably different, which suggests that four micro-continental blocks (termed the Yinshan, Ordos, Longgang and Nangrim blocks) separated by three Paleoproterozoic tectonic belts (include the Khondalite Belt, Jiao-Liao-Ji Belt and Trans-North China

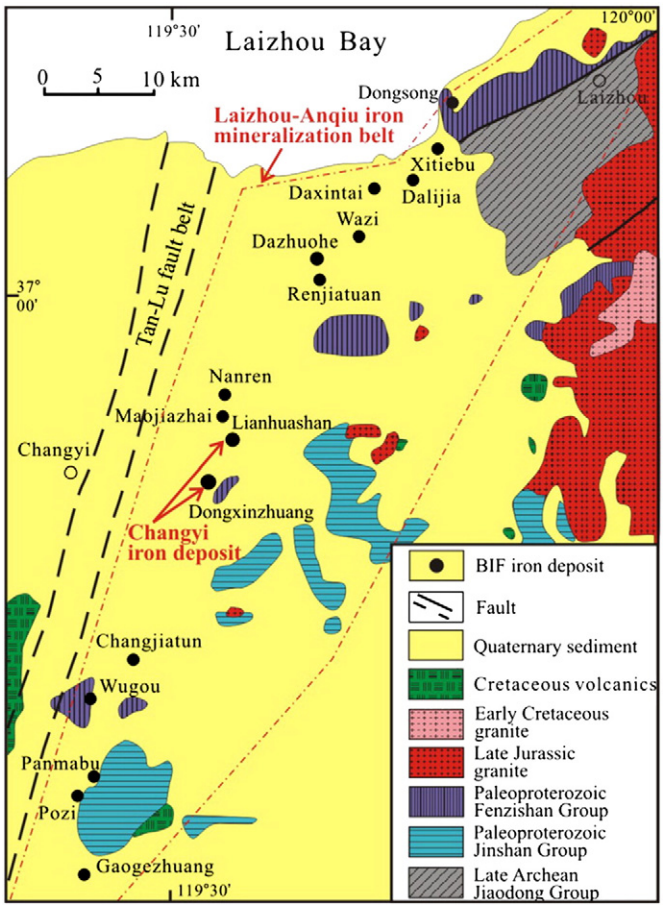

Fig. 2. Geological map of the Laizhou-Anqiu iron mineralization belt showing distribution of the BIF iron deposits (modified after Xu et al., 2011).

Orogen) constructed the NCC through collision during Paleoproterozoic, among which the Yinshan Block collided with the Ordos Block to form the Western Block along the Khondalite Belt at ca. 1.95 Ga and the Longgang Block collided with the Nangrim Block to form the Eastern Block along the Jiao-Liao-Ji Belt at ca. 1.90 Ga (Zhao et al., 2005, 2012). The final cratonization of the NCC was accomplished by the collision between the Eastern and Western blocks along the Trans-North China Orogen at ca. 1.85 Ga (Zhao et al., 2005, 2012). Therefore, the Paleoproterozoic tectonic environment of the NCC, oceans between independent continental blocks or rifts within a coherent continent, is one of the most important issues that these models argued. The subsequent evolution of the NCC remained largely stable until Mesozoic, prior to the reactivation, large-scale replacement and substantial thinning of the lithosphere (e.g., Chen, 2010; Gao et al., 2002; Griffin et al., 1998; Menzies and Xu, 1998; Zhang et al., 2011a).

The present study area in the eastern Shandong Province is located within the Paleoproterozoic Liaoji Orogenic belt (Fig. 1). Archean to Paleoproterozoic sequences constitute the basements of this area. The Archean sequence is mainly represented by the Jiaodong Group, which is as old as 2.7 Ga and consists of TTG gneisses with supracrustal rocks such as amphibolite, biotite-plagioclase gneiss, biotite leptite, and leuco-leptite (Jahn et al., 2008; Wang et al., 2009). These rocks have been generally metamorphosed to amphibolite facies, and locally to granulite facies (Jahn et al., 2008). The Paleoproterozoic sequences are represented by the Jingshan and Fenzishan Group. The former unconformably overlies the Archean TTG gneisses and is mainly composed of sillimanite–biotite–quartz schist, biotite leptite and graphite-bearing gneisses with some marble and amphibolite, metamorphosed under upper amphibolite to granulite facies conditions (Jahn et al., 2008; Wang et al., 2009). Detrital zircons from a two mica–sillimanite–garnet gneiss show a range of ages from 2.2 to 2.9 Ga, indicating that deposition of the Jingshan Group occurred after 2.2 Ga (Wan et al., 2006). The Fenzishan Group is mainly distributed to the west of the Jingshan Group and consists of biotite leptynite, magnetite quartzite, sillimanite–biotite schist, marble and amphibolite, similar to those of the Jingshan Group, but at a slightly lower metamorphic grade of amphibolite facies (Wang et al., 2009). A garnet–muscovite–quartz schist from the Fenzishan Group shows detrital zircons with a range of ages between 2.2 and 2.9 Ga (Wan et al., 2006), also similar to those of the Jingshan Group. The basement rocks are extensively invaded by late Jurassic granites and early Cretaceous granodiorites (Yang et al., 2012).

A prominent magnetic anomaly belt termed the Laizhou-Anqiu iron mineralization belt has been demarcated within the Paleoproterozoic sequences (especially in the Fenzishan Group) at the northwestern Jiaobei terrain of eastern Shandong Province (Fig. 2). Several small-scale BIF deposits are distributed within this magnetic anomaly belt. As the largest among these, the Changyi BIF deposit is being mined for iron resources.

3. Geology of the Changyi BIF

The Changyi BIF occurs within the Paleoproterozoic Fenzishan Group, and the BIF bands are interbedded with metamorphic rocks. The BIF bands can be divided into macrobands, mesobands and microbands based on their scale and occurrence. The macrobands are composed of alternating quartz-rich light and magnetite-rich dark mesobands and are layered or lens-shaped with thickness of several centimeters up to thirty six meters and length of ten meters to longer than two kilometers. The mesobands are constituted by alternating magnetite-rich and quartz-rich microbands. The microbands show thickness varying from 1 mm to 9 mm with major constituents of magnetite (15 to 65 vol.%), quartz (25 to 65 vol.%) and amphibole (15 to 30 vol.%). Occasionally, garnet, epidote, chlorite, calcite, biotite and pyrite occur. Detailed descriptions of the BIF bands were reported in Lan et al. (2013).

Three major types of metamorphic wallrocks of the Changyi BIF are identified, including plagioclase gneisses and leptynites, garnet-bearing gneisses and amphibolites. These rocks are interbedded with each other and generally show gneissic structures with horizontal occurrence, although locally modified by faults and granites. The plagioclase gneisses (Fig. 3a) and leptynites (Fig. 3b) are mainly composed of plagioclase (25 to 65 vol.%), quartz (30 to 60 vol.%) and biotite (5 to 25 vol.%). The garnet-bearing gneisses (Fig. 3c) show wide variation of mineral components, which mainly consist of garnet (almandine in composition, 3 to 30 vol.%), quartz (25 to 45 vol.%), plagioclase (<40 vol.%) and alternatively biotite (<30 vol.%) and amphibole (<40 vol.%). The amphibolites are constituted by dominant amphibole (60 to 95 vol.%) with subordinate plagioclase (5 to 35 vol.%) and biotite (<35 vol.%) (Fig. 3d). The amphiboles are compositionally ferrohornblende–magnesiohornblende. Combined with chemical compositions, the associations of amphibole and garnet suggest that the Changyi BIF and its wallrocks have suffered amphibolite facies metamorphism (Lan et al., 2012, 2013).

4. Sample description and analytical procedures

4.1. Sample description

In order to constrain the source materials of the metamorphic rocks, two plagioclase gneisses (CY2-01 and CY2-83) and one garnet-bearing gneiss (CY2-40) were selected for LA-ICP-MS zircon U–Pb dating. These samples were collected from the depths of −150 m (CY2-01), −190 m (CY2-40) and −270 m (CY2-83) in the mining tunnels, respectively. Nine samples of the pagioclase gneisses and leptynites, six samples of the garnet-bearing gneisses and six samples of the

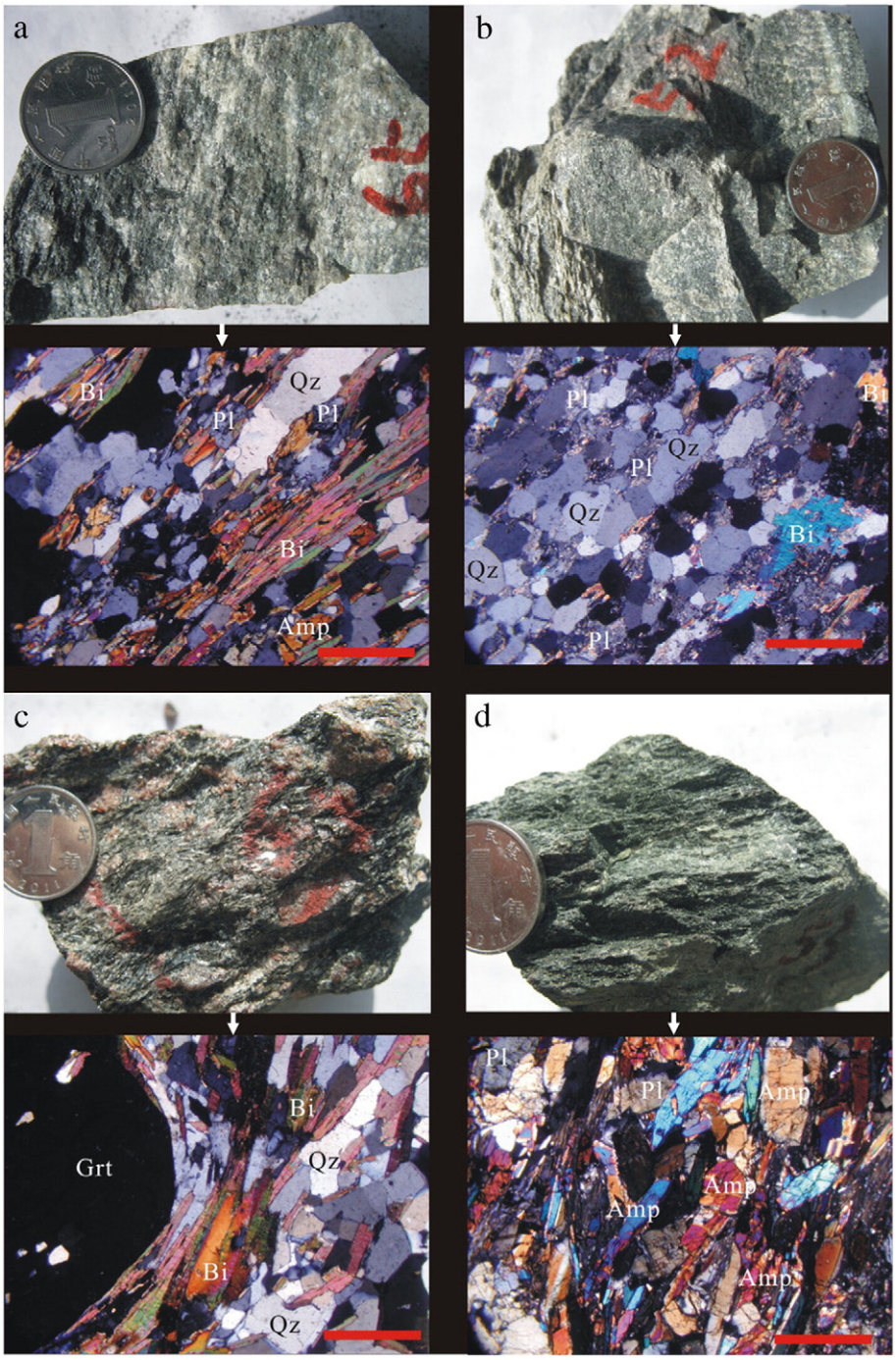

Fig. 3. Representative hand-specimen photos and micrographs of the plagioclase gneisses (a), leptynites (b), garnet-bearing gneisses (c) and amphibolites (d). The scale bar is 0.5 mm in the micrograph. Qz—quartz; Pl—plagioclase; Amp—amphibole; Bi—biotite; Grt—garnet.

amphibolites were selected for whole-rock major and trace element analysis. These samples were also collected from the depths varying from −150 m to −270 m. Ten samples of these rocks were measured for Sr–Nd isotopic compositions. These samples, which are fresh and unaltered, were crushed into 200 mesh for major and trace elements as well as Sr–Nd isotopes measurement.

4.2. Analytical procedures

4.2.1. Zircon U–Pb dating and in situ Hf isotopic analyses

U–Pb dating and trace element analyses of zircon were conducted synchronously by LA-ICP-MS at the State Key Laboratory of Geological Processes and Mineral Resources, China University of Geosciences, Wuhan. The operating conditions for the laser ablation system and the ICP-MS instrument and data reduction are similar to those described by Liu et al. (2008). Laser sampling was performed using a GeoLas 2005 coupled with an Agilent 7500a ICP-MS instrument. A laser spot size of 32 μm and a laser repetition of 6 Hz were used during the analyses. Quantitative calibration for trace element analyses and U–Pb dating were performed by *ICPMSDataCal* Liu et al. (2008). Zircon 91500 was used as external standard for U–Pb dating, and was analyzed twice every 5 analyses. Concordia diagrams and weighted mean calculations were made using Isoplot/Ex_ver 3 (Ludwig, 2003).

Table 1
LA-ICP-MS zircon U–Pb data for the metamorphic rocks from the Changyi BIF deposit.

Spot	Concentrations (ppm)				Isotopic ratios						Isotopic ages (Ma)					
	Pb	Th	U	Th/U	$^{207}Pb/^{206}Pb$	1σ	$^{207}Pb/^{235}U$	1σ	$^{206}Pb/^{238}U$	1σ	$^{207}Pb/^{206}Pb$	1σ	$^{207}Pb/^{235}U$	1σ	$^{206}Pb/^{238}U$	1σ
CY2-01 (Plagioclase gneiss, this study)																
1	71	42	90	0.46	0.2132	0.0053	16.9747	0.4273	0.5757	0.0059	2931	35	2933	24	2931	24
2	86	51	109	0.47	0.2151	0.0048	17.1869	0.3763	0.5781	0.0052	2944	35	2945	21	2941	21
3	105	92	127	0.72	0.2104	0.0043	16.6765	0.3345	0.5721	0.0046	2909	33	2916	19	2917	19
4	54	41	66	0.62	0.2138	0.0050	17.1054	0.3991	0.5774	0.0060	2935	38	2941	22	2938	25
5	96	75	119	0.63	0.2113	0.0050	16.9362	0.4031	0.5774	0.0056	2917	39	2931	23	2938	23
6	51	29	64	0.45	0.2178	0.0055	17.6240	0.4249	0.5834	0.0058	2965	40	2969	23	2962	24
7	49	32	64	0.50	0.2144	0.0051	17.2033	0.3973	0.5783	0.0065	2939	38	2946	22	2942	26
8	51	40	66	0.60	0.2107	0.0047	16.7973	0.3594	0.5739	0.0053	2922	36	2923	21	2924	22
9	60	42	79	0.53	0.2135	0.0047	17.1682	0.3650	0.5784	0.0053	2932	36	2944	20	2942	22
10	151	165	187	0.88	0.2113	0.0048	16.9363	0.3790	0.5756	0.0070	2916	38	2931	21	2931	28
11	108	86	143	0.60	0.2112	0.0049	16.8522	0.3725	0.5731	0.0055	2915	37	2926	21	2921	23
12	509	4	1222	0.00	0.1539	0.0030	7.9413	0.1530	0.3707	0.0033	2391	33	2224	17	2033	16
13	5	0	9	0.02	0.1700	0.0098	11.2388	0.6657	0.4879	0.0136	2558	96	2543	55	2562	59
14	163	163	203	0.80	0.2121	0.0041	16.9917	0.3453	0.5765	0.0056	2922	31	2934	19	2935	23
15	82	53	105	0.50	0.2155	0.0051	17.3045	0.4024	0.5797	0.0053	2947	39	2952	22	2947	22
16	49	29	63	0.47	0.2123	0.0057	16.8531	0.4551	0.5740	0.0063	2923	44	2927	26	2924	26
17	54	34	70	0.48	0.2136	0.0051	16.9983	0.4002	0.5757	0.0058	2933	39	2935	23	2931	24
18	58	47	76	0.63	0.2147	0.0053	17.1302	0.4481	0.5774	0.0087	2943	39	2942	25	2938	35
19	33	26	42	0.61	0.2117	0.0050	16.7722	0.3916	0.5735	0.0061	2920	38	2922	22	2922	25
20	82	88	98	0.90	0.2135	0.0044	17.0332	0.3639	0.5758	0.0054	2932	33	2937	20	2931	22
21	51	32	67	0.47	0.2146	0.0047	17.1595	0.3748	0.5779	0.0053	2943	35	2944	21	2940	22
22	176	134	230	0.58	0.2086	0.0057	16.3887	0.4444	0.5666	0.0072	2895	45	2900	26	2894	30
23	194	135	258	0.52	0.2049	0.0051	16.0247	0.4245	0.5621	0.0079	2866	41	2878	25	2875	33
24	188	141	252	0.56	0.2029	0.0059	15.6689	0.4375	0.5570	0.0095	2849	47	2857	27	2854	40
25	141	63	191	0.33	0.2062	0.0062	16.6372	0.5271	0.5761	0.0090	2876	48	2914	30	2933	37
26	199	106	278	0.38	0.2031	0.0066	15.7580	0.4915	0.5575	0.0087	2852	54	2862	30	2856	36
27	161	146	223	0.65	0.1991	0.0062	15.2546	0.4553	0.5512	0.0094	2820	50	2831	28	2830	39
28	259	258	334	0.77	0.1998	0.0054	15.7408	0.4312	0.5637	0.0078	2825	44	2861	26	2882	32
29	170	109	240	0.46	0.2000	0.0056	15.5569	0.3962	0.5584	0.0094	2828	46	2850	24	2860	39
30	208	129	280	0.46	0.2047	0.0038	16.2814	0.3464	0.5677	0.0075	2865	30	2893	20	2898	31
31	156	96	212	0.45	0.2000	0.0038	15.8008	0.3169	0.5641	0.0061	2828	31	2865	19	2884	25
32	147	89	197	0.45	0.2035	0.0047	16.0113	0.3801	0.5625	0.0089	2855	37	2877	23	2877	37
33	189	113	250	0.45	0.2068	0.0042	16.5327	0.3674	0.5702	0.0063	2881	33	2908	21	2909	26
34	187	132	238	0.55	0.2097	0.0056	16.7881	0.4669	0.5732	0.0083	2903	44	2923	27	2921	34
35	163	119	204	0.58	0.2133	0.0054	17.3132	0.4544	0.5805	0.0074	2931	36	2952	25	2951	30
36	140	84	181	0.46	0.2102	0.0070	16.7550	0.5252	0.5736	0.0084	2906	54	2921	30	2923	35
37	275	200	354	0.57	0.2075	0.0068	16.3792	0.5379	0.5669	0.0098	2886	53	2899	31	2895	40
CY2-40 (Garnet-bearing gneiss, this study)																
1	388	220	496	0.44	0.2159	0.0055	17.4253	0.4543	0.5810	0.0075	2950	41	2959	25	2953	31
2	488	82	663	0.12	0.2155	0.0051	17.4251	0.4079	0.5812	0.0057	2947	38	2959	22	2953	23
3	308	123	435	0.28	0.2048	0.0053	16.0316	0.4382	0.5630	0.0085	2865	43	2879	26	2879	35
4	562	515	744	0.69	0.1933	0.0050	14.5256	0.3665	0.5399	0.0063	2772	42	2785	24	2783	26
5	228	109	293	0.37	0.2158	0.0064	17.5106	0.5159	0.5833	0.0082	2950	48	2963	28	2962	34
6	509	247	660	0.37	0.2088	0.0056	16.6604	0.4478	0.5713	0.0073	2898	43	2915	26	2913	30
7	441	363	606	0.60	0.1872	0.0046	13.8939	0.3436	0.5302	0.0062	2718	40	2743	23	2742	26
8	72	33	85	0.38	0.2131	0.0072	18.5855	0.6068	0.6269	0.0115	2929	54	3021	31	3137	45
9	426	287	520	0.55	0.2127	0.0055	17.3235	0.4338	0.5800	0.0059	2928	42	2953	24	2949	24
10	204	122	254	0.48	0.2128	0.0066	17.3337	0.5144	0.5803	0.0074	2927	50	2953	28	2950	30
11	230	116	290	0.40	0.2131	0.0066	17.3516	0.5166	0.5807	0.0077	2929	55	2954	29	2952	32
12	704	234	1020	0.23	0.1871	0.0046	13.7800	0.3262	0.5250	0.0049	2716	41	2735	22	2720	21
13	1051	536	1477	0.36	0.1872	0.0042	13.9056	0.3080	0.5301	0.0052	2718	37	2743	21	2742	22
14	260	158	321	0.49	0.2122	0.0054	17.1725	0.4530	0.5789	0.0072	2924	42	2945	25	2944	29
15	475	256	576	0.45	0.2158	0.0053	17.6540	0.4413	0.5850	0.0067	2950	40	2971	24	2969	27
16	671	412	858	0.48	0.2012	0.0054	15.5779	0.4314	0.5558	0.0078	2836	44	2851	26	2849	32
17	629	1810	454	3.98	0.2049	0.0051	16.0443	0.4018	0.5627	0.0064	2866	41	2879	24	2878	27
18	652	71	906	0.08	0.2053	0.0048	16.1635	0.4328	0.5652	0.0094	2869	38	2887	26	2888	39
19	411	195	521	0.37	0.2062	0.0047	16.1755	0.3597	0.5645	0.0055	2876	37	2887	21	2885	23
20	799	839	1007	0.83	0.1872	0.0042	13.7540	0.3134	0.5278	0.0056	2718	37	2733	22	2732	24
21	547	503	682	0.74	0.1910	0.0045	14.2257	0.3376	0.5354	0.0055	2750	33	2765	23	2764	23
22	1425	1093	2135	0.51	0.1873	0.0044	12.4670	0.2926	0.4788	0.0048	2718	39	2640	22	2522	21
23	442	246	528	0.46	0.2138	0.0055	17.2035	0.4402	0.5788	0.0059	2934	42	2946	25	2944	24
24	516	248	621	0.40	0.2134	0.0058	17.1647	0.4592	0.5782	0.0056	2932	44	2944	26	2942	23
CY2-65 (Amphibole-bearing biotite plagioclase gneiss, Lan et al., 2013)																
1	295	140	404	0.35	0.2035	0.0056	15.8407	0.4241	0.5597	0.0065	2855	45	2867	26	2865	27
2	89	449	73	6.15	0.1410	0.0077	8.1732	0.4226	0.4239	0.0097	2240	95	2250	47	2278	44
3	156	180	218	0.83	0.1793	0.0045	12.6660	0.3069	0.5085	0.0064	2647	41	2655	23	2650	27
4	557	99	796	0.12	0.2020	0.0049	15.7471	0.3641	0.5583	0.0052	2842	39	2862	22	2859	22
5	806	184	1251	0.15	0.1854	0.0050	13.6292	0.3769	0.5254	0.0070	2702	45	2724	26	2722	30
6	388	80	564	0.14	0.1951	0.0057	14.8663	0.4131	0.5455	0.0061	2787	47	2807	26	2806	25
7	92	157	132	1.18	0.1569	0.0050	10.0931	0.3375	0.4616	0.0080	2433	54	2443	31	2446	35
8	695	157	1020	0.15	0.1916	0.0047	14.4588	0.3463	0.5396	0.0064	2767	39	2780	23	2782	27
9	364	43	531	0.08	0.1932	0.0052	14.6153	0.3723	0.5420	0.0064	2769	44	2791	24	2792	27

Table 1 (*continued*)

Spot	Concentrations (ppm)				Isotopic ratios						Isotopic ages (Ma)					
	Pb	Th	U	Th/U	$^{207}Pb/^{206}Pb$	1σ	$^{207}Pb/^{235}U$	1σ	$^{206}Pb/^{238}U$	1σ	$^{207}Pb/^{206}Pb$	1σ	$^{207}Pb/^{235}U$	1σ	$^{206}Pb/^{238}U$	1σ
10	241	177	314	0.56	0.1978	0.0063	15.2831	0.4735	0.5514	0.0070	2809	52	2833	30	2831	29
11	349	218	511	0.43	0.1794	0.0058	12.8413	0.3921	0.5127	0.0069	2647	53	2668	29	2668	29
12	738	166	1059	0.16	0.1978	0.0051	15.2066	0.3873	0.5496	0.0059	2809	42	2828	24	2824	24
13	562	124	844	0.15	0.1887	0.0046	14.0311	0.3431	0.5320	0.0052	2731	41	2752	23	2750	22
14	94	511	72	7.12	0.1415	0.0061	8.1376	0.3469	0.4159	0.0088	2246	76	2246	39	2242	40
15	776	121	1177	0.10	0.1914	0.0058	14.2399	0.4334	0.5330	0.0062	2754	49	2766	29	2754	26
16	557	111	791	0.14	0.2045	0.0064	15.9978	0.5084	0.5608	0.0067	2862	51	2877	30	2870	28
17	92	508	74	6.82	0.1413	0.0065	7.8403	0.3760	0.3991	0.0066	2244	80	2213	43	2165	30
18	587	134	877	0.15	0.1912	0.0051	14.3425	0.3834	0.5385	0.0055	2754	43	2773	25	2777	23
19	442	113	617	0.18	0.2075	0.0053	16.3499	0.4373	0.5656	0.0068	2886	42	2897	26	2890	28
20	576	161	847	0.19	0.1936	0.0049	14.5834	0.3666	0.5410	0.0056	2773	41	2788	24	2787	23
21	338	183	559	0.33	0.1643	0.0044	10.9220	0.2924	0.4774	0.0055	2502	45	2517	25	2516	24
22	574	279	815	0.34	0.1913	0.0057	14.2711	0.4115	0.5367	0.0062	2753	82	2768	27	2770	26
CY2-83 (Plagioclase gneiss, this study)																
1	351	169	456	0.37	0.2205	0.0056	17.9503	0.4591	0.5893	0.0060	2984	40	2987	25	2987	24
2	1079	900	1483	0.61	0.1952	0.0046	14.6362	0.3592	0.5421	0.0057	2787	38	2792	23	2792	24
3	923	610	1230	0.50	0.2130	0.0051	16.9347	0.4310	0.5762	0.0071	2928	40	2931	24	2933	29
4	462	252	615	0.41	0.2189	0.0059	17.7411	0.5027	0.5865	0.0076	2973	44	2976	27	2975	31
5	1212	431	1720	0.25	0.2138	0.0062	17.0399	0.5058	0.5769	0.0073	2935	47	2937	28	2936	30
6	1101	636	1437	0.44	0.2266	0.0065	18.8873	0.6079	0.6019	0.0112	3028	45	3036	31	3038	45
7	569	526	706	0.75	0.2129	0.0053	17.3760	0.4606	0.5882	0.0081	2928	41	2956	25	2982	33
8	691	842	807	1.04	0.2202	0.0054	18.1287	0.4739	0.5920	0.0083	2982	40	2997	25	2997	34
9	824	926	1011	0.92	0.2133	0.0052	17.1415	0.4014	0.5768	0.0055	2931	40	2943	22	2936	22
10	834	459	1093	0.42	0.2139	0.0058	17.3835	0.4683	0.5807	0.0071	2935	49	2956	26	2952	29
11	722	287	976	0.29	0.2133	0.0058	17.3422	0.4632	0.5807	0.0064	2931	43	2954	26	2951	26
12	913	1294	1093	1.18	0.2068	0.0050	16.4505	0.4116	0.5692	0.0076	2881	40	2903	24	2905	31
13	613	270	815	0.33	0.2104	0.0050	17.5743	0.4614	0.5976	0.0090	2908	39	2967	25	3020	36
14	826	397	1147	0.35	0.2111	0.0048	16.9869	0.4199	0.5760	0.0077	2914	37	2934	24	2933	31
15	461	332	488	0.68	0.2258	0.0059	20.7246	0.5510	0.6584	0.0085	3033	42	3126	26	3261	33
16	899	660	1212	0.54	0.2061	0.0055	16.1660	0.4417	0.5631	0.0072	2875	43	2887	26	2880	30
17	563	271	741	0.37	0.2191	0.0059	18.0415	0.5183	0.5906	0.0089	2976	43	2992	28	2992	36
18	503	328	654	0.50	0.2069	0.0052	16.5806	0.4276	0.5756	0.0076	2881	41	2911	25	2931	31
19	149	83	195	0.43	0.2132	0.0057	17.0873	0.4962	0.5759	0.0089	2931	43	2940	28	2932	36
20	1068	811	1518	0.53	0.1875	0.0044	13.8293	0.3461	0.5288	0.0066	2720	39	2738	24	2736	28
21	641	368	836	0.44	0.2072	0.0053	16.6338	0.4368	0.5770	0.0082	2884	41	2914	25	2936	34
22	1137	1170	1527	0.77	0.1871	0.0049	13.7580	0.3548	0.5276	0.0051	2717	44	2733	24	2731	21

In-situ zircon Hf isotopic analyses were conducted on the same spots analyzed for U–Pb dating. Hf isotopic compositions were determined by a Neptune MC-ICP-MS equipped with a GeolasPlus 193 nm ArF excimer laser at the Institute of Geology and Geophysics, Chinese Academy of Sciences (IGGCAS). Laser spot size of 40 μm and laser repetition of 8 Hz were used during the analyses. The signal collection model is one block with 200 cycles, with an integration time of 0.131 s for one cycle and a total time of 26 s during each analysis. Zircon 91500 was used as external standard for Hf isotopic analyses and was analyzed twice every 5 analyses. Repeated analyses of 91500 yielded a mean $^{176}Hf/^{177}Hf$ ratio of 0.282297 ± 25 (2σ) which is concordant with the $^{176}Hf/^{177}Hf$ ratios measured by Goolaerts et al. (2004) and Woodhead et al. (2004). The detailed analytical procedures were described in Xie et al. (2008).

4.2.2. Major and trace elements

Major and trace elements were analyzed in the Rock-Mineral Preparation and Analysis Laboratory and the Metallogenic Geochronology Laboratory at the IGGCAS, respectively. For major elements analyses, mixtures of whole-rock powder (0.5 g) and $Li_2B_4O_7$ + $LiBO_2$ (5 g) were made into glass disks and analyzed by X-ray fluorescence spectroscopy (XRF) with an AXIOS Minerals spectrometer. The analytical uncertainties are better than 4% for all the major elements. For trace element analyses, whole-rock powder (40 mg) were dissolved in distilled HF + HNO_3 in Teflon screw-cap capsules at 200 °C for 5 days, dried, and then digested with HNO_3 at 150 °C for 1 day. The final step was repeated once. Dissolved samples were diluted to 49 ml with 1% HNO_3 and 1 ml 500 ppb indium was added to the solution as an internal standard. Trace element abundances were determined by inductively coupled plasma mass spectrometry (ICP-MS) using a Finnigan MAT Element spectrometer. A blank solution was prepared and the total procedural blank was <100 ng for all trace elements. Multi-element standard solution was measured for matrix effects and instrument drift correction. Precision for all trace elements is estimated to be 5% and accuracy is better than 5% for most of the elements.

4.2.3. Whole-rock Sr–Nd isotopes

Whole-rock powder for Sr and Nd isotopic analyses were dissolved in Teflon bombs after being spiked with ^{87}Rb, ^{84}Sr, ^{149}Sm and ^{150}Nd tracers prior to HF + HNO_3 + $HClO_4$ dissolution. Rb, Sr, Sm and Nd were separated using conventional ion exchange procedures and measured using a Finnigan MAT262 multi-collector mass spectrometer at the IGGCAS. Procedural blanks are <100 pg for Sm and Nd and <300 pg for Rb and Sr. The isotopic ratios were corrected for mass fractionation by normalizing to $^{86}Sr/^{88}Sr = 0.1194$ and $^{146}Nd/^{144}Nd = 0.7219$, respectively. The measured values for the JNdi-1 Nd standard and NBS987 Sr standard were $^{143}Nd/^{144}Nd = 0.512108 \pm 11$ (2σ, n = 5) and $^{87}Sr/^{86}Sr = 0.710256 \pm 11$ (2σ, n = 5), respectively. USGS reference material BCR-2 was measured to monitor the accuracy of the analytical procedures, with the following results: $^{143}Nd/^{144}Nd = 0.512633 \pm 13$ (2σ) and $^{87}Sr/^{86}Sr = 0.705035 \pm 12$ (2σ).

5. Results

5.1. Zircon U–Pb dating

Three samples of the plagioclase gneisses (CY2-01 and CY2-83) and the garnet-bearing gneiss (CY2-40) were selected for LA-ICP-MS zircon U–Pb dating. The U–Pb analytical data are presented in Table 1.

Most of the zircon grains in the CY2-01 are rounded with distinct to indistinct oscillatory zoning in cathodoluminescence (CL) images (Fig. 4a). 35 analyses of the 37 spots show comparatively high Th/U ratios (from 0.33 to 0.90) (Table 1) and fall on the concordia line (Fig. 4b). Their $^{207}Pb/^{206}Pb$ ages vary from 2820 Ma to 2965 Ma. Combined with the rounded shapes and the high Th/U ratios, they are interpreted as detrital zircons possessing magmatic genesis. The other two analyses have much younger $^{207}Pb/^{206}Pb$ ages (2391 to 2558 Ma) and show dramatically low Th/U ratios (0.003 to 0.02), which are also interpreted as detrital zircons but with metamorphic origin.

Zircon grains in the CY2-40 are complex, showing euhedral to anhedral shapes with wide variation of grain size (Fig. 4a). Generally, these zircons are smaller than those of the CY2-01. They are commonly dark to gray in CL images with some showing white thin rims. The thin rims have no oscillatory zoning and display irregular shapes, which are considered to be produced by deuteric metamorphism or alteration. 25 spots conducted on the dark or gray domains yield $^{207}Pb/^{206}Pb$ ages varying from 2716 Ma to 2950 Ma, mainly grouping into 2716–2718 Ma, 2866–2876 Ma and 2924–2950 Ma (Table 1). These zircons show wide variation of Th/U ratios (0.08 to 3.98) and inner textures, which can be attributed to multiple origins (both magmatic and metamorphic zircons are present) or deuteric modification. However, some zircons showing large difference in Th/U ratios and inner textures also have similar $^{207}Pb/^{206}Pb$ ages and fall on the concordia line (for example, spots 17, 18 and 19, Table 1 and Fig. 4c), indicating that the widely varied Th/U ratios are most likely attributed to the multiple origins of the zircons. Therefore, combined with the variable ages and shapes, these zircons are interpreted as detrital zircons irrespective of their magmatic or metamorphic origins. Notably, the zircons showing white thin rims should be modified by a deuteric event. It is a pity that this event could not be dated due to the poor overgrowth. Nonetheless, it could be associated with the regional amphibolite facies metamorphism occurring at ca. 1.8–1.9 Ga, as also recorded by the BIF bands (Lan et al., 2013) and the similar metamorphic rocks (Wan et al., 2006) in this region.

Zircon grains in the CY2-83 have large difference in size with euhedral to anhedral shapes. Most of the zircon grains are rounded. They are dark to gray in CL images and commonly show distinct oscillatory zoning (Fig. 4a). Some of them probably experienced slight to moderate modification due to the altered features in their rims. 22 analyses conducted on 22 grains yield $^{207}Pb/^{206}Pb$ ages varying from 2717 Ma to 3033 Ma with relatively high Th/U ratios (0.25 to 1.18). All the grains fall on the concordia line except one showing $^{207}Pb/^{206}Pb$ age of 3033 Ma (Fig. 4d). Considering the rounded shapes as well as the distinct oscillatory zoning and the high Th/U ratios, these zircons are interpreted as detrital zircons having magmatic origins, although some of them were probably modified by deuteric event more or less.

5.2. Major elements

Major elements analyses are presented in Table 2. Different types of rocks show obvious difference in major elements compositions. Generally, the plagioclase gneisses and leptynites have the highest contents of SiO_2 (57.4 to 76.7 wt.%) and Na_2O (0.76 to 4.81 wt.%), the garnet-bearing gneisses show the highest TFe_2O_3 contents (10.9 to 30.8 wt.%), and the amphibolites are characterized by the lowest SiO_2 (46.5 to 52.8 wt.%) and the highest MgO (5.68 to 10.9 wt.%) and CaO (7.46 to 9.78 wt.%) contents (Fig. 5). There are no systematic difference in TiO_2 (0.23 to 1.36 wt.%), Al_2O_3 (9.35 to 17.0 wt.%), MnO (0.02 to 1.33 wt.%), K_2O (0.27 to 2.48 wt.%) and P_2O_5 (0.03 to 0.68 wt.%) contents among the three types of rocks (Fig. 5). It is notable that the major elements of the amphibolites show narrow variation while the other two types have large variation in some elements.

5.3. Trace and rare earth elements

Trace and rare earth elements analyses are presented in Table 3 and shown in Fig. 6. Notably, the trace and rare earth elements are much more homogeneous in the amphibolites than those in the other two types.

5.3.1. Transition metals

Generally, the amphibolites have the highest contents of the transition metals such as V (averaging 237 ppm), Co (averaging 52 ppm), Sc (averaging 38 ppm) and Zn (averaging 83 ppm), whereas the garnet-bearing gneisses hold the highest contents of Cr (averaging 426 ppm), Ni (averaging 145 ppm) and Cu (83 ppm) (Table 3). The plagioclase gneisses and leptynites obtain the lowest contents of all the transition metals. Since most of the transition metals have close relationships with MgO and FeO, the above distribution features are consistent with the highest MgO contents (averaging 8.0%) in the amphibolites and the highest TFe_2O_3 contents (averaging 23%) in the garnet-bearing gneisses. The high concentration of the transition metals (except for Cu) in the amphibolites are similar to those of the basalts (such as MORB and CAB, Kelemen et al., 2007), whereas the low contents in the plagioclase gneisses and leptynites show certain affinities to the post-Archean Australian Shale (PAAS, McLennan, 1989) or the North American Shale Composite (NASC, Gromet et al., 1984).

5.3.2. High field strength elements (HFSEs)

On the Primitive Mantle (PM) normalized trace element diagrams (Fig. 6a, c, e), all the rocks show Nb and Ta depletion with Nb/Ta ratios increasing from the garnet-bearing gneisses (averaging 11.6) and the plagioclase gneisses and leptynites (averaging 12.5) to the amphibolites (averaging 15.9). The low Nb/Ta ratios in the garnet-bearing gneisses (averaging 11.6) and the plagioclase gneisses and leptynites are similar to those of the NASC (11.6, Gromet et al., 1984) and the continental crust (12–13, Barth et al., 2000), whereas the relatively high Nb/Ta ratios in the amphibolites are close to that of the MORB (16.7 ± 1.8, Kamber and Collerson, 2000). The garnet-bearing gneisses and amphibolites commonly show Zr and Hf depletion (Fig. 6b, c) while the plagioclase gneisses and leptynites display Zr and Hf enrichment (Fig. 6a).

5.3.3. Large ion lithophile elements (LILEs)

The garnet-bearing gneisses commonly show the highest Rb contents, consistent with the extensive existence of biotite in this type of rocks. The amphibolites have the lowest and widely varied Rb contents. Ba varies widely in all the rocks. On the PM normalized trace element diagrams, Sr generally shows positive and negative anomalies in the amphibolites and the garnet-bearing gneisses, respectively. No obvious Sr anomalies are observed in the plagioclase gneisses and leptynites. Th and U generally show positive anomalies in the garnet-bearing gneisses and the plagioclase gneisses and leptynites, which are obviously different from the negative Th anomalies in the amphibolites (Fig. 6c). In addition, the amphibolites have the lowest Th and U contents.

5.3.4. Rare earth elements (REEs)

All the rocks show LREE enrichment relative to HREE with the $(La/Yb)_N$ ratios increasing from the amphibolites (averaging 3.28) to the garnet-bearing gneisses (averaging 11.2) and the plagioclase gneisses and leptynites (averaging 12.9). The amphibolites are characterized by the lowest contents of REE ($\sum$REE = 41–95 ppm, averaging 73 ppm) while the plagioclase gneisses and leptynites ($\sum$REE = 59–404 ppm, averaging 154 ppm) and the garnet-bearing gneisses ($\sum$REE = 74–410 ppm, averaging 136 ppm) show higher REE contents. Positive Eu anomalies are observed in the amphibolites, whereas the other two types commonly show no Eu anomalies. This feature is well consistent with the highest contents of plagioclase, CaO and Sr in the amphibolites.

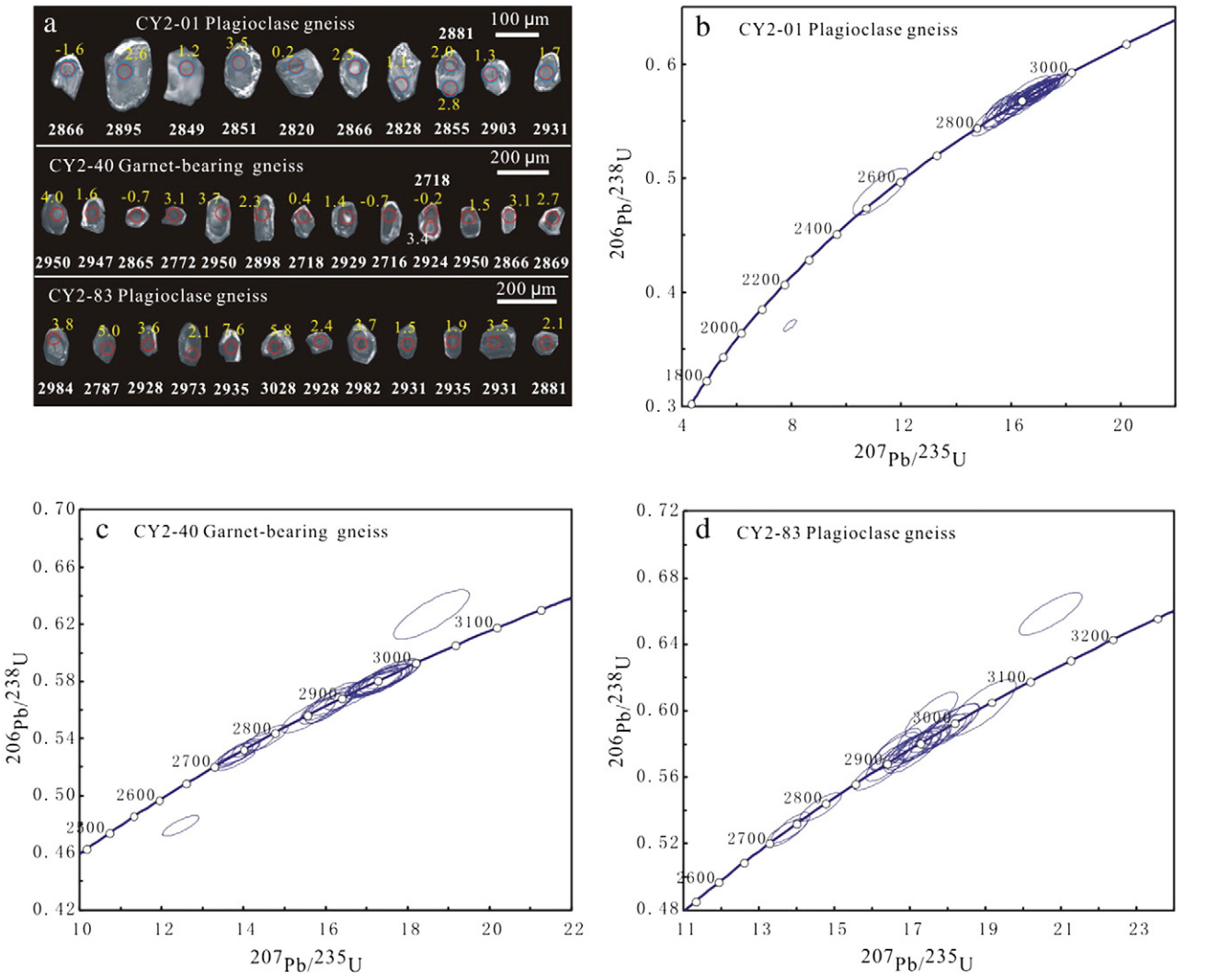

Fig. 4. Representative CL images of zircon grains from the metamorphic rocks (a) and LA–ICPMS zircon U–Pb concordia diagrams of the plagioclase gneisses (b and d) and the garnet-bearing gneiss (c). $^{207}Pb/^{206}Pb$ age (Ma) and $\varepsilon_{Hf}(t)$ value are also shown.

5.4. Sr–Nd–Hf isotopes

Whole-rock Rb–Sr and Sm–Nd isotopic compositions were analyzed from ten samples, which show systematic variation among the three types of rocks (Table 4). The Rb contents, $^{87}Rb/^{86}Sr$ and $^{87}Sr/^{86}Sr$ ratios increase from the amphibolites (Rb = 5.5–30 ppm, $^{87}Rb/^{86}Sr$ = 0.08–0.70, $^{87}Sr/^{86}Sr$ = 0.708291–0.726511) to the plagioclase gneisses and leptynites (Rb = 35–66 ppm, $^{87}Rb/^{86}Sr$ = 0.25–0.99, $^{87}Sr/^{86}Sr$ = 0.711727–0.748833) and the garnet-bearing gneisses (Rb = 92–94 ppm, $^{87}Rb/^{86}Sr$ = 1.45–1.69, $^{87}Sr/^{86}Sr$ = 0.753220–0.789250). The Sr contents, however, are similar in the garnet-bearing gneisses (123–207 ppm) and the amphibolites (158–190 ppm) while the plagioclase gneisses and leptynites have the highest (168–410 ppm). For the Sm–Nd isotopes, increasing of $^{147}Sm/^{144}Nd$ and $^{143}Nd/^{144}Nd$ ratios with decreasing Nd contents from the plagioclase gneisses and leptynites (Nd = 19.1–66.2 ppm, $^{147}Sm/^{144}Nd$ = 0.0860–0.1121, $^{143}Nd/^{144}Nd$ = 0.510650–0.511007) to the garnet-bearing gneisses (Nd = 12.9–13.6 ppm, $^{147}Sm/^{144}Nd$ = 0.1096–0.1291, $^{143}Nd/^{144}Nd$ = 0.511076–0.511241) and the amphibolites (Nd = 8.02–13.4 ppm, $^{147}Sm/^{144}Nd$ = 0.1493–0.1631 $^{143}Nd/^{144}Nd$ = 0.511721–0.512085) is observed. The plagioclase gneisses and leptynites have the highest Sm contents (3.11–9.40 ppm), whereas the other two types show lower and similar Sm contents (2.10–3.30 ppm). Single-stage Nd depleted mantle model ages (T_{DM}) are 2902–3214 Ma, 3017–3414 Ma and 2964–3354 Ma in the plagioclase gneisses and leptynites, garnet-bearing gneisses and amphibolites, respectively.

Zircons with the age range of 2716–2950 Ma from the garnet-bearing gneiss (CY2-40) yield $\varepsilon_{Hf}(t)$ values varying from −0.7 to 4.0. The corresponding Hf depleted mantle model ages (T_{DM}) range from 2915 Ma to 3151 Ma. Zircons (2717–3033 Ma) in the plagioclase gneiss (CY2-83) have similar $\varepsilon_{Hf}(t)$ values and T_{DM} to those of the garnet-bearing gneiss, showing $\varepsilon_{Hf}(t)$ values of 0.8–7.6 and T_{DM} of 2867–3199 Ma (Fig. 10 and Table 5).

6. Discussion

6.1. Protoliths of the metamorphic rocks

6.1.1. Element mobility evaluation

Isochemical metamorphism should be evaluated before protolith interpretation being carried out. In the case of the metamorphic rocks from the Changyi BIF deposit, which have been metamorphosed under amphibolite facies conditions (Lan et al., 2012, 2013), the mobility of major and trace elements of these rocks should be carefully treated due to the medium-grade metamorphism. Former studies have revealed that major elements (Si, Al, Mg, Fe, Ca, Na and P), transition

Table 2
Major elements contents (wt.%) of the metamorphic rocks from the Changyi BIF deposit.

Sample	Depth	SiO_2	TiO_2	Al_2O_3	FeO	$Fe_2O_3^T$	MnO	MgO	CaO	Na_2O	K_2O	P_2O_5	LOI	Total
Plagioclase gneisses and leptynites														
CY2-01	−150 m	65.7	0.68	15.5	3.65	5.23	0.07	2.44	3.81	3.62	1.50	0.21	1.88	100.6
CY2-03	−150 m	67.8	0.37	16.2	2.62	3.47	0.04	1.60	3.46	4.81	1.12	0.15	0.76	99.8
CY2-07	−150 m	76.6	0.23	10.5	2.71	3.96	0.05	1.72	3.55	0.76	1.63	0.05	1.04	100.0
CY2-14	−150 m	68.4	0.53	15.7	4.85	6.30	0.13	1.92	2.88	1.91	1.57	0.19	0.78	100.4
CY2-46	−190 m	57.4	1.36	12.7	8.82	15.2	0.23	3.00	5.35	0.97	2.19	0.18	1.42	99.9
CY2-65	−190 m	74.1	0.45	9.40	4.59	6.61	0.07	2.56	3.49	1.64	0.96	0.04	0.70	100.0
CY2-82	−230 m	76.7	0.37	10.6	3.24	4.42	0.02	0.95	1.36	3.00	1.54	0.05	0.48	99.5
CY2-83	−270 m	61.4	0.58	17.0	5.33	6.86	0.08	3.24	3.20	3.76	2.24	0.13	1.34	99.8
CY2-88	−270 m	68.8	0.47	14.9	2.56	3.87	0.04	1.52	2.00	4.44	2.30	0.15	1.52	100.0
Garnet-bearing gneisses														
CY2-10	−150 m	43.9	0.98	16.4	25.3	30.8	1.33	1.55	4.59	0.20	0.27	0.68	−1.18	99.5
CY2-15	−150 m	57.2	0.61	15.2	8.05	10.9	0.13	5.06	3.45	1.96	2.48	0.12	2.20	99.3
CY2-28	−150 m	43.6	0.53	14.0	20.2	27.1	0.75	3.57	6.99	0.22	0.36	0.09	2.14	99.4
CY2-37	−190 m	51.8	0.27	12.1	19.5	25.3	0.13	2.57	3.90	0.71	1.68	0.08	0.74	99.2
CY2-56	−190 m	53.4	0.44	13.9	17.8	23.4	0.11	2.63	2.13	0.62	2.10	0.07	−0.24	98.6
CY2-67	−190 m	56.8	0.35	13.5	16.1	20.2	0.07	2.53	1.24	1.20	2.03	0.07	−0.10	97.9
Amphibolites														
CY2-09	−150 m	52.8	1.04	13.7	8.36	13.1	0.19	5.68	8.86	2.30	0.76	0.12	0.84	99.4
CY2-20	−150 m	50.0	0.49	14.6	7.80	12.1	0.12	8.41	9.34	2.55	0.38	0.03	1.12	99.2
CY2-23	−150 m	47.3	0.72	14.5	9.73	14.6	0.17	8.47	8.22	2.09	0.75	0.08	2.64	99.5
CY2-53	−190 m	46.5	0.99	12.0	8.82	12.7	0.18	10.92	9.43	0.93	1.59	0.17	3.20	98.7
CY2-59	−190 m	52.1	0.89	13.9	8.75	12.2	0.18	6.77	9.78	2.12	0.43	0.10	0.70	99.2
CY2-87	−270 m	51.2	0.66	15.1	8.15	11.0	0.19	7.77	9.40	1.96	0.96	0.07	1.08	99.3
GSR1	Ref.	73.10	0.28	13.4		2.13	0.06	0.41	1.54	3.11	5.02	0.09	0.69	99.80
	Mea.	72.80	0.28	13.4		2.14	0.06	0.42	1.55	3.13	5.01	0.09	0.69	99.60

LOI: loss on ignition. GSR1 is Chinese granite standard. Ref.: recommended value for reference standard. Mea.: the measured value for the reference standard during the analytical procedures.

metals (Ni, Co, Cr, Ti, Sc, V, Mn, Zn and Cu), HFSEs (Zr, Hf, Y and Nb) and REEs can remain constant during gabbro-amphibolite transformation (Alirezaei and Cameron, 2002). Isochemical or nearly isochemical metamorphism has also been observed in marine sediments subjected to low- to high-grade metamorphism during orogenic metamorphism (Garofalo, 2012). These results suggest that most geochemical features of different types of rocks can still survive in medium-grade metamorphism. HFSEs and REEs have long been considered to be immobile during secondary alteration and metamorphism (Drury, 1978; Floyd and Winchester, 1978; Pearce and Norry, 1979; Schüssler et al., 1989; Smalley and Field, 1991; Taylor et al., 1986; Winchester and Floyd, 1976), and therefore they can be applied to constrain the origin of metamorphic rocks even experienced granulite facies metamorphism (e.g., Drury, 1978; Green et al., 1972; Jahn and Zhang, 1984). LILEs (such as K, Rb, Ba, Th and U), however, are commonly considered to be more mobile. Because of the mobility, these elements are good indicators to detect metamorphic effects on the rocks (e.g., Fernandes et al., 1987; Rudnick et al., 1985; Smalley et al., 1983). K/Rb, Th/U and La/Th ratios are usually invoked to test the mobility of the LILEs (e.g., Bauernhofer et al., 2009; Rudnick et al., 1985; Shaw, 1968; Sighinolfi, 1969; Smalley et al., 1983; Stephenson, 2000). Metamorphic rocks experienced high-grade metamorphism commonly show higher and increasing K/Rb ratios with decreasing K contents (e.g., ≥500 for granulite, Rudnick et al., 1985; Sighinolfi, 1969), whereas unmetamorphosed rocks of igneous rocks (averaging about 230, except for ocean tholeiites, Rudnick et al., 1985; Shaw, 1968) and shales (averaging about 200, Rudnick et al., 1985) show lower and relatively constant K/Rb ratios. The K/Rb ratios of the metamorphic rocks from the Changyi BIF deposit vary from 171 to 1025, most of which plot within the trend of K/Rb ratios observed in igneous rocks in the K_2O vs. Rb diagram (Fig. 7a), suggesting that these metamorphic rocks may have not suffered significant K and Rb loss. One plagioclase gneiss sample

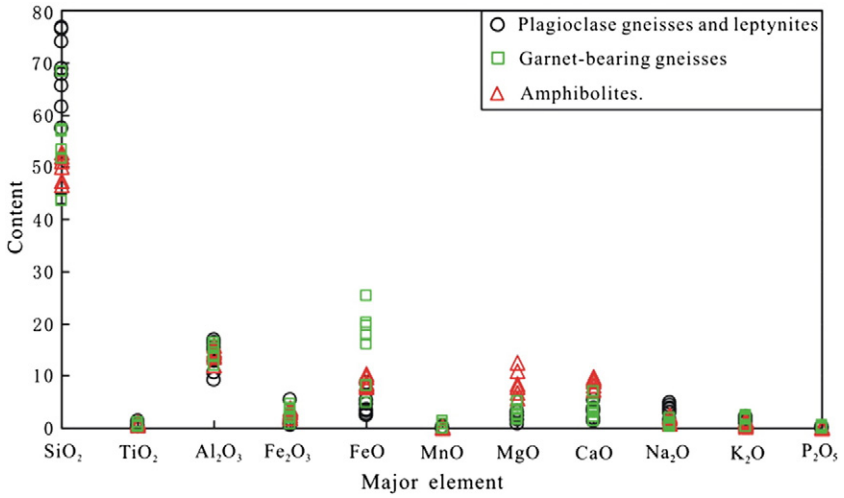

Fig. 5. Major elements contents of the plagioclase gneisses and leptynites, garnet-bearing gneisses and amphibolites.

Table 3
Trace and rare earth elements concentration (ppm) of the metamorphic rocks from the Changyi BIF deposit.

	Plagioclase gneisses and leptynites									Garnet-bearing gneisses						Amphibolites						GSR1	
	CY2-01	−03	−07	−14	−46	−65	−82	−83	−88	−10	−15	−28	−37	−56	−67	−9	−20	−23	−53	−59	−87	Ref.	Mea.
Sc	11.9	3.81	5.95	9.39	35.9	10.2	5.16	14.4	5.20	27.8	20.7	14.2	14.6	13.2	14.2	42.1	34.7	41.3	26	41.2	43.3	6.1	6.01
Cr	254	199	304	270	165	297	308	289	180	658	463	349	376	374	336	112	284	309	793	143	170	5	4.78
Co	17.6	12.7	11.8	11.4	44.1	15.4	8.91	21.9	9.77	79.2	33.3	13.9	16.6	14.8	15.6	53.1	45.4	50.5	64.3	48.2	51.4	3.4	3.35
Ni	26.7	23.7	30.5	28.1	3.80	23.0	27.0	77.3	14.5	395	189	83.3	52.6	76.6	71.3	27.8	106	83.4	346	42.6	55.7	2.3	2.37
Cu	71.2	11.6	2.6	4.74	24.9	9.36	4.54	17.4	5.44	370	19.3	2.4	56.9	50	2.33	86.1	7.08	52.8	2.1	26.8	18.4	3.2	2.40
Zn	45.9	48.4	25.3	17.4	127	47.3	24.6	23.6	38.8	69.1	20.5	66.7	57.1	46.4	56.8	113	55.7	76.6	101	90.2	63.8	28	27.6
Ga	17.4	17.6	12.0	19.0	23.3	14.8	12	20.8	19.2	8.74	21.8	16.2	11	15.7	19.0	19.8	13.1	15.7	17.7	18.1	15.8	19	19.1
Rb	60.4	10.9	85.5	46.5	128	54.7	57.3	51.0	52.3	10.0	102	8.46	84	91.2	95.4	28.4	9.23	23.5	56.2	6.3	31.1	466	465
Sr	253	364	121	125	196	163	179	168	342	21.4	168	71.2	23.6	134	185	210	228	224	104	179	119	106	109
Cs	3.22	3.46	4.08	4.38	4.76	3.44	3.83	3.27	1.64	0.57	11.6	2.84	5.9	6.92	5.91	1.47	1.15	1.30	2.11	0.49	1.42	38.4	38.2
Ba	211	418	245	230	503	887	6353	301	1045	114	651	55.2	365	4801	616	439	143	142	407	94.1	107	343	343
Nb	8.54	5.61	2.78	8.99	7.27	4.16	2.65	5.60	6.00	5.72	5.64	4.18	3.42	3.06	3.3	5.05	2.34	3.20	5.65	3.53	1.83	40	38.5
Ta	0.69	0.41	0.24	0.69	0.56	0.24	0.26	0.59	0.52	0.38	0.52	0.37	0.28	0.32	0.32	0.31	0.13	0.19	0.4	0.25	0.12	7.2	7.36
Zr	187	135	103	169	147	560	95.7	142	151	144	109	83.0	36.5	51.7	49.0	108	30.7	49.3	68.3	74.7	40.1	167	164
Hf	4.77	3.79	2.90	4.79	4.30	19.9	2.51	4.03	3.94	3.61	3.25	2.51	1.16	1.53	1.44	3.03	1.02	1.54	1.95	2.11	1.17	6.3	6.35
La	26.9	27.9	18.5	16.9	24.1	86.4	12.8	26.7	34.3	83.1	15.7	21.3	17.9	14.2	15.7	12.0	4.08	5.55	13.5	9.95	4.91	54	54.7
Ce	53.5	54.4	31.9	32.7	46.1	166	22.7	48.5	56.7	172	28.8	37.6	29.7	25.0	27.4	24.9	8.9	12.9	27.7	18.8	10.7	108	109
Pr	6.31	6.16	3.70	3.79	5.92	19.91	2.69	5.67	6.51	19.2	3.55	4.52	3.67	3.10	3.37	3.24	1.19	1.69	3.85	2.76	1.45	12.7	13.3
Nd	22.2	20.7	12.3	13.6	22.6	70.1	9.13	19.8	21.4	68.1	12.9	16	13.6	11.8	12.2	13.2	5.42	7.39	15.9	11.5	6.45	47	47.4
Sm	4.35	3.94	2.39	2.93	5.23	10.85	1.75	3.84	3.64	11.88	2.97	2.96	2.47	2.30	2.54	3.45	1.54	2.13	4.00	3.00	1.78	9.7	9.75
Eu	1.18	1.05	0.65	0.89	1.5	1.79	0.49	1.02	0.89	2.81	0.97	1.23	0.97	0.72	0.78	1.18	0.65	0.84	1.27	0.97	0.74	0.85	0.83
Gd	3.64	2.68	1.77	2.79	5.43	8.13	1.32	3.18	2.87	8.98	2.75	2.41	2.74	2.26	2.18	3.82	1.83	2.56	3.66	3.34	2.20	9.3	9.37
Tb	0.55	0.34	0.26	0.50	0.90	0.97	0.18	0.45	0.40	1.17	0.45	0.31	0.44	0.32	0.33	0.66	0.33	0.45	0.56	0.61	0.41	1.65	1.63
Dy	2.95	1.55	1.50	3.17	5.55	5.13	1.04	2.35	2.26	6.03	2.70	1.56	2.67	1.75	1.97	4.30	2.17	3.02	3.04	3.98	2.81	10.2	10.1
Ho	0.51	0.28	0.29	0.66	1.15	1.11	0.20	0.46	0.43	1.16	0.55	0.3	0.57	0.35	0.40	0.92	0.48	0.65	0.58	0.85	0.60	2.05	2.10
Er	1.24	0.71	0.80	1.70	3.28	3.39	0.55	1.18	1.15	3.19	1.54	0.85	1.6	0.96	1.09	2.57	1.4	1.88	1.45	2.41	1.67	6.5	6.34
Tm	0.17	0.11	0.12	0.24	0.51	0.57	0.09	0.17	0.18	0.47	0.24	0.14	0.25	0.15	0.17	0.39	0.21	0.28	0.2	0.38	0.25	1.06	1.03
Yb	1.08	0.73	0.79	1.5	3.23	4.32	0.59	1.09	1.15	3.15	1.57	0.93	1.56	0.98	1.08	2.57	1.37	1.90	1.19	2.44	1.61	7.4	7.31
Lu	0.16	0.12	0.13	0.22	0.51	0.78	0.10	0.17	0.17	0.49	0.24	0.16	0.24	0.16	0.17	0.39	0.21	0.30	0.18	0.38	0.25	1.15	1.12
Y	12.4	6.86	7.00	16.3	28.7	24.4	5.42	11.8	11.3	28.7	15.0	8.8	18.1	9.87	12.0	21.9	11.2	15.8	13.8	21.6	15.0	62	59.0
U	1.19	1.75	1.99	1.39	1.16	1.09	1.37	2.48	7.49	1.94	2.04	3.7	0.93	1.09	1.37	0.37	0.13	0.11	0.44	0.27	0.13	18.8	18.9
Th	5.50	7.76	4.80	5.69	4.50	18.6	4.73	8.35	11.3	18.6	7.70	10.00	4.72	5.37	5.07	1.64	0.26	0.35	1.48	1.26	0.44	54	54.9
Pb	7.65	14.3	4.88	6.84	11.4	5.94	10.17	6.50	11.2	5.04	6.28	3.27	3.64	5.01	4.44	5.46	3.67	5.24	2.06	4.18	3.81	31	32.0

GSR1 is Chinese granite standard. Ref.: recommended value for reference standard. Mea.: the measured value for the reference standard during the analytical procedures.

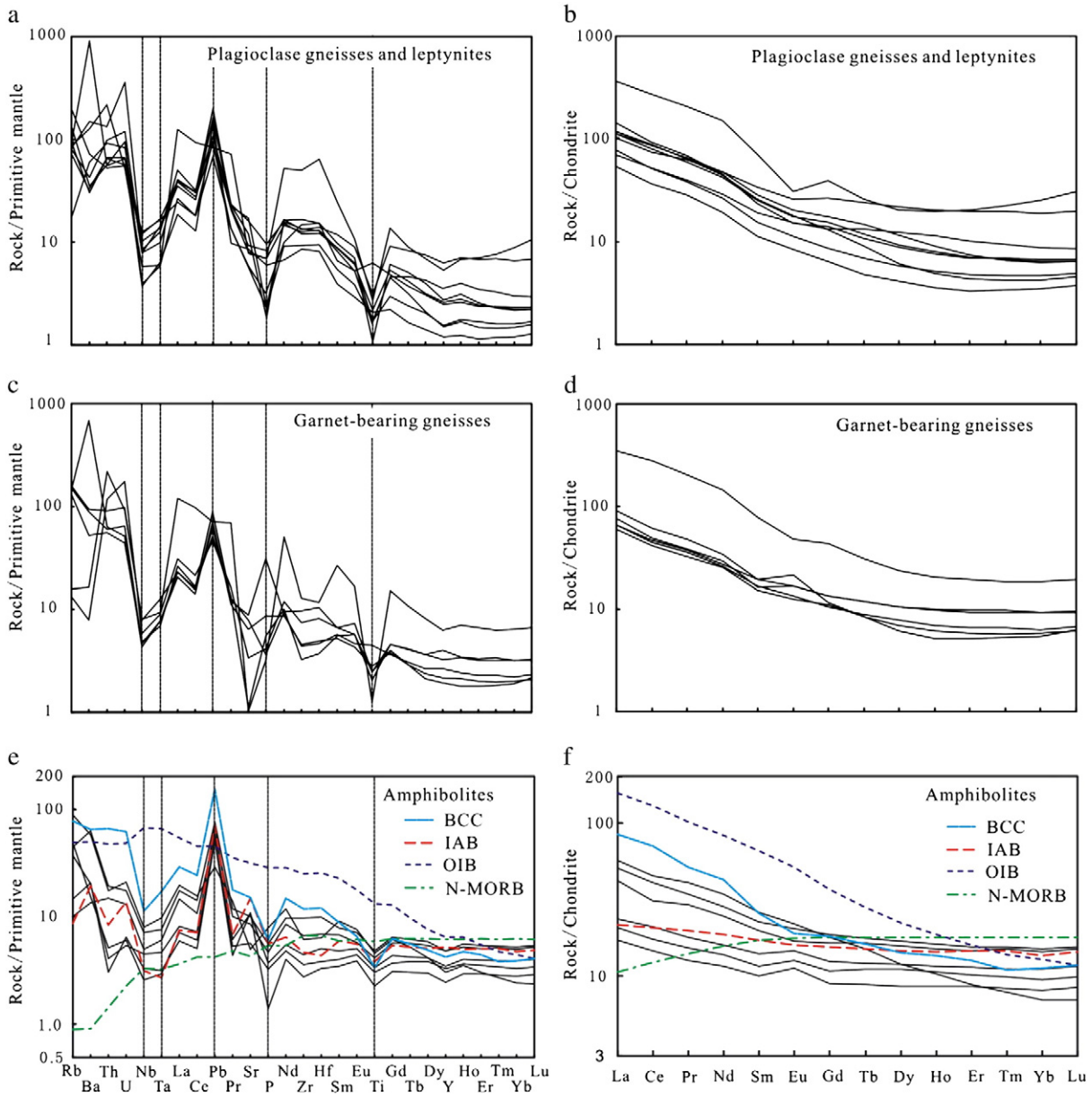

Fig. 6. Primitive Mantle (PM) normalized trace element diagrams and Chondrite-normalized REE patterns for the plagioclase gneisses (a, b), garnet-bearing gneisses (c, d) and amphibolites (e, f). Bulk continental crust (BCC), island arc basalts (IAB), ocean island basalts (OIB) and normal-type mid-ocean ridge basalts (N-MORB) are shown for comparison. The values of PM, Chondrite, OIB and N-MORB are from Sun and McDonough (1989). The IAB is from Takanashi et al. (2011), and the BCC is from Rudnick and Gao (2003).

Table 4
Sr–Nd isotopic compositions of the metamorphic rocks from the Changyi BIF deposit.

	Age (Ma)	Rb (ppm)	Sr (ppm)	$^{87}Rb/^{86}Sr$	$^{87}Sr/^{86}Sr$	$\pm2\sigma$	$(^{87}Sr/^{86}Sr)_i$	Sm (ppm)	Nd (ppm)	$^{147}Sm/^{144}Nd$	$^{143}Nd/^{144}Nd$	$\pm2\sigma$	$\varepsilon_{Nd}(t)$	$\int_{Sm/Nd}$	T_{DM} (Ma)
Plagioclase gneisses and leptynites															
CY2-1	2220	57.4	249	0.6678	0.729040	13	0.707654	4.05	21.8	0.1121	0.510992	13	−8.0	−0.43	3214
CY2-3	2220	35.1	410	0.2476	0.711727	10	0.703798	3.11	19.1	0.0986	0.510944	12	−5.1	−0.50	2902
CY2-65	2220	53.7	168	0.9311	0.739873	14	0.710054	9.40	66.2	0.0860	0.510650	12	−7.2	−0.56	2965
CY2-83	2220	66.2	195	0.9891	0.748833	11	0.717157	4.42	25.3	0.1059	0.511007	13	−5.9	−0.46	3008
Garnet-bearing gneisses															
CY2-15	2220	92.2	158	1.6949	0.753220	11	0.698940	2.76	12.9	0.1291	0.511241	10	−8.0	−0.34	3414
CY2-67	2220	93.9	190	1.4459	0.789250	13	0.742944	2.46	13.6	0.1096	0.511076	16	−5.7	−0.44	3017
Amphibolites															
CY2-9	2220	26.1	200	0.3774	0.715246	11	0.703159	3.30	13.4	0.1493	0.511721	15	−4.4	−0.24	3354
CY2-23	2220	21.1	207	0.2954	0.712586	12	0.703127	2.25	8.37	0.1631	0.512085	11	−1.2	−0.17	3185
CY2-59	2220	5.50	190	0.0841	0.708291	10	0.705597	3.01	12.0	0.1522	0.511879	11	−2.1	−0.23	3129
CY2-87	2220	29.6	123	0.7011	0.726511	11	0.704058	2.10	8.02	0.1583	0.512066	14	−0.2	−0.20	2964

Chondrite Uniform Reservoir (CHUR) values ($^{87}Rb/^{86}Sr = 0.0847$, $^{87}Sr/^{86}Sr = 0.7045$, $^{147}Sm/^{144}Nd = 0.1967$, $^{143}Nd/^{144}Nd = 0.512638$) are used for the calculation. $\lambda_{Rb} = 1.42 \times 10^{-11}$ year^{-1}, $\lambda_{Sm} = 6.54 \times 10^{-12}$ year^{-1} (Lugmair and Harti, 1978). $\lambda_{U238} = 1.55125 \times 10^{-10}$ year^{-1}, $\lambda_{U235} = 9.8485 \times 10^{-10}$ year^{-1}, $\lambda_{Th232} = 4.9475 \times 10^{-11}$ year^{-1} (Steiger and Jäger, 1977). Since the protoliths of these metamorphic rocks were deposited or emplaced during ca. 2191 and 2240 Ma (Lan et al., 2013), the initial $^{87}Sr/^{86}Sr$ and $^{143}Nd/^{144}Nd$ ratios were calculated using an eclectic age of 2220 Ma.

Table 5
LA-ICP-MS zircon Hf isotopic compositions for the metamorphic rocks from the Changyi BIF deposit.

Spot no.	Age (Ma)	$^{176}Yb/^{177}Hf$	$^{176}Lu/^{177}Hf$	$^{176}Hf/^{177}Hf$	2σ	$\varepsilon_{Hf}(0)$	$\varepsilon_{Hf}(t)$	T_{DM1} (Ma)	T_{DM2} (Ma)	$f_{Lu/Hf}$
CY2-40 (Garnet-bearing gneiss, this study)										
01	2950	0.038531	0.001143	0.281072	0.000015	−60.1	4.0	3047	3104	−0.97
02	2947	0.014646	0.000481	0.280968	0.000012	−63.8	1.6	3133	3249	−0.99
03	2865	0.025747	0.000875	0.280979	0.000025	−63.4	−0.7	3151	3324	−0.97
04	2772	0.023682	0.000738	0.281138	0.000013	−57.8	3.1	2926	3019	−0.98
05	2950	0.019695	0.000612	0.281032	0.000015	−61.5	3.7	3058	3124	−0.98
06	2898	0.028621	0.000904	0.281042	0.000017	−61.2	2.3	3068	3171	−0.97
07	2718	0.027885	0.000949	0.281106	0.000022	−58.9	0.4	2985	3146	−0.97
08	2929	0.020402	0.000601	0.280980	0.000015	−63.4	1.4	3127	3249	−0.98
09	2928	0.032148	0.000963	0.281039	0.000016	−61.3	2.7	3077	3167	−0.97
10	2927	0.022997	0.000783	0.281033	0.000017	−61.5	2.8	3071	3158	−0.98
11	2929	0.015229	0.000483	0.281036	0.000014	−61.4	3.6	3043	3113	−0.99
12	2716	0.005102	0.000156	0.281035	0.000011	−61.4	−0.7	3019	3210	−1.00
13	2718	0.015008	0.000520	0.281067	0.000023	−60.3	−0.2	3005	3183	−0.98
14	2924	0.025329	0.000799	0.281051	0.000021	−60.9	3.4	3047	3122	−0.98
15	2950	0.038502	0.001231	0.281006	0.000017	−62.5	1.5	3143	3257	−0.96
16	2836	0.029799	0.000925	0.281061	0.000016	−60.5	1.5	3044	3168	−0.97
17	2866	0.031889	0.000914	0.281086	0.000017	−59.6	3.1	3009	3095	−0.97
18	2869	0.023264	0.000751	0.281066	0.000013	−60.3	2.7	3024	3119	−0.98
19	2876	0.025336	0.000788	0.281058	0.000014	−60.6	2.6	3037	3134	−0.98
20	2718	0.027887	0.000935	0.281145	0.000017	−57.5	1.8	2931	3059	−0.97
21	2750	0.024032	0.000787	0.281133	0.000014	−58.0	2.4	2936	3049	−0.98
22	2718	0.027268	0.000825	0.281151	0.000017	−57.3	2.2	2915	3035	−0.98
23	2934	0.032206	0.000953	0.281072	0.000013	−60.1	4.0	3031	3090	−0.97
24	2932	0.062526	0.001850	0.281089	0.000018	−59.5	2.8	3081	3164	−0.94
CY2-65 (Amphibole-bearing biotite plagioclase gneiss, Lan et al., 2013)										
01	2855	0.033901	0.001014	0.281104	0.000013	−59.0	3.3	2993	3076	−0.97
02	2240	0.059988	0.001679	0.281638	0.000016	−40.1	7.5	2304	2341	−0.95
03	2647	0.029492	0.000870	0.281269	0.000016	−53.1	4.7	2758	2825	−0.97
04	2842	0.032763	0.000998	0.281079	0.000015	−59.9	2.2	3025	3134	−0.97
05	2702	0.032700	0.000973	0.281110	0.000012	−58.8	0.1	2982	3149	−0.97
06	2787	0.024119	0.000727	0.281065	0.000015	−60.4	0.9	3023	3167	−0.98
07	2433	0.028615	0.000851	0.281325	0.000023	−51.2	1.9	2681	2831	−0.97
08	2767	0.035986	0.001121	0.281107	0.000025	−58.9	1.2	2997	3134	−0.97
09	2769	0.044872	0.001334	0.281128	0.000019	−58.1	1.6	2985	3110	−0.96
10	2809	0.075642	0.002163	0.281084	0.000028	−59.7	−0.6	3112	3279	−0.93
11	2647	0.010647	0.000304	0.281122	0.000019	−58.4	0.5	2915	3083	−0.99
12	2809	0.043550	0.001346	0.281078	0.000020	−59.9	0.7	3054	3197	−0.96
13	2731	0.034328	0.001092	0.281075	0.000020	−60.0	−0.7	3038	3220	−0.97
14	2246	0.061734	0.001782	0.281683	0.000021	−38.5	9.1	2246	2247	−0.95
15	2754	0.024004	0.000619	0.281176	0.000021	−56.4	4.3	2866	2934	−0.98
16	2862	0.024626	0.000769	0.281073	0.000021	−60.1	2.8	3016	3110	−0.98
17	2244	0.050692	0.001485	0.281679	0.000018	−38.7	9.3	2235	2229	−0.96
18	2754	0.025745	0.000765	0.281253	0.000022	−53.7	6.8	2772	2784	−0.98
19	2886	0.018945	0.000598	0.281091	0.000021	−59.5	4.3	2979	3036	−0.98
20	2773	0.009497	0.000248	0.281110	0.000019	−58.8	3.1	2927	3023	−0.99
21	2502	0.010942	0.000351	0.281261	0.000021	−53.4	2.1	2732	2876	−0.99
22	2753	0.026509	0.000711	0.281117	0.000019	−58.5	2.0	2952	3074	−0.98
CY2-83 (Plagioclase gneiss, this study)										
01	2984	0.016553	0.000522	0.281008	0.000027	−62.4	3.8	3083	3144	−0.98
02	2787	0.032567	0.001069	0.281200	0.000034	−55.6	5.0	2867	2915	−0.97
03	2928	0.023663	0.000762	0.281052	0.000029	−60.8	3.6	3043	3113	−0.98
04	2973	0.018625	0.000600	0.280972	0.000022	−63.7	2.1	3138	3239	−0.98
05	2935	0.007385	0.000236	0.281131	0.000033	−58.0	7.6	2897	2873	−0.99
06	3028	0.065824	0.002041	0.281126	0.000024	−58.2	5.8	3045	3054	−0.94
07	2928	0.042189	0.001437	0.281058	0.000023	−60.6	2.4	3090	3183	−0.96
08	2982	0.049961	0.001574	0.281068	0.000020	−60.3	3.7	3087	3147	−0.95
09	2931	0.047525	0.001529	0.281036	0.000035	−61.4	1.5	3126	3239	−0.95
10	2935	0.021141	0.000716	0.280999	0.000023	−62.7	1.9	3111	3219	−0.98
11	2931	0.023218	0.000715	0.281046	0.000022	−61.0	3.5	3047	3118	−0.98
12	2881	0.030565	0.000966	0.281051	0.000019	−60.9	2.1	3061	3169	−0.97
13	2908	0.020702	0.000661	0.281044	0.000020	−61.1	3.1	3046	3130	−0.98
14	2914	0.027451	0.000851	0.281064	0.000019	−60.4	3.5	3034	3107	−0.97
15	3033	0.038928	0.001224	0.280965	0.000021	−63.9	1.9	3199	3297	−0.96
16	2875	0.031639	0.001021	0.281058	0.000028	−60.6	2.1	3055	3163	−0.97
17	2976	0.034588	0.001071	0.280997	0.000017	−62.8	2.1	3142	3241	−0.97
18	2881	0.045693	0.001499	0.281044	0.000023	−61.1	0.8	3113	3246	−0.95
19	2931	0.033434	0.000969	0.281037	0.000018	−61.4	2.7	3080	3169	−0.97
20	2720	0.025752	0.000877	0.281125	0.000019	−58.3	1.2	2954	3095	−0.97
21	2884	0.023682	0.000709	0.281038	0.000020	−61.3	2.2	3058	3164	−0.98
22	2717	0.016332	0.000507	0.281095	0.000017	−59.3	0.8	2966	3120	−0.98

The following parameters were applied to calculation: $(^{176}Lu/^{177}Hf)_{CHUR} = 0.0332$, $(^{176}Hf/^{177}Hf)_{CHUR,0} = 0.282772$, $(^{176}Lu/^{177}Hf)_{DM} = 0.0384$, $(^{176}Hf/^{177}Hf)_{DM,0} = 0.28325$ (Blichert-Toft and Albaréde, 1997; Griffin et al., 2000), ^{176}Lu decay constant $\lambda = 1.867 \times 10^{-11}$ a^{-1} (Söderlund et al., 2004).

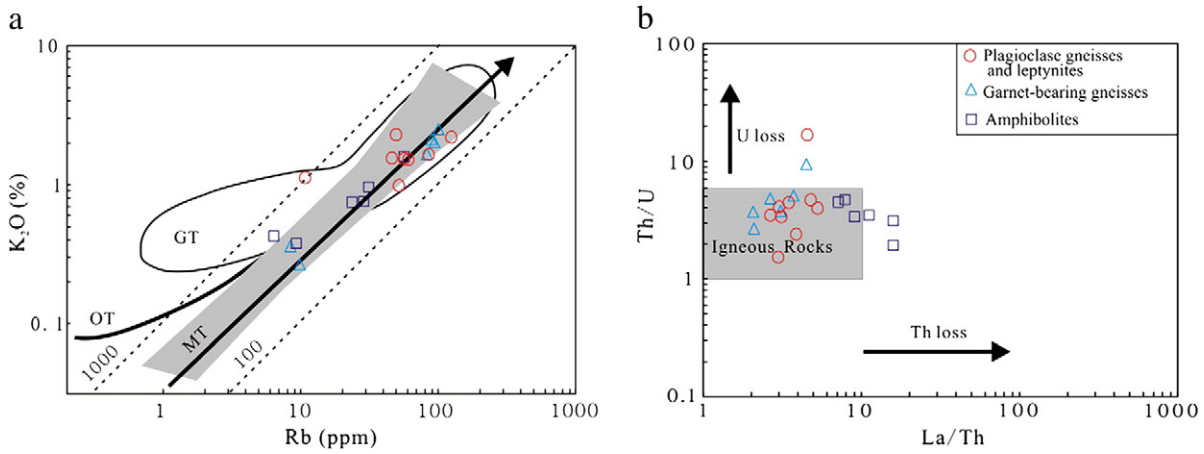

Fig. 7. K_2O vs. Rb (a) and Th/U vs. La/Th (b) diagrams for element mobility evaluation. (a) and (b) are after Rudnick et al. (1985). MT, main trend, obtained from igneous rocks; OT, ocean tholeiite trend; GT, granulite trend. Shaded field surrounding MT line represents field of 12 linear regressions which were averaged by Shaw (1968) to obtain the MT line.

has remarkably high K/Rb ratio (1025) and falls into the trend of the granulite (Fig. 7a), implying that this sample was probably modified locally. Similarly, the La/Th vs. Th/U diagram also suggests that most of the metamorphic rocks in this study have not suffered U and Th loss, although individual samples of the gneisses indeed show certain U loss (Fig. 7b). Since MORBs have higher La/Th ratios (La/Th > 10, Rudnick et al., 1985), the relatively high La/Th ratios (7.30–16.1, averaging 11.3) of the amphibolites could be correct (e.g., Bauernhofer et al., 2009). Conclusively, the stable features of the mobile elements (LILEs) in most samples of the metamorphic rocks from the Changyi BIF deposit suggest that these metamorphic rocks may have mostly kept their original chemical compositions. In addition, no significant pegmatite veins and fluid alteration observed in these metamorphic rocks also provide petrographic evidence for isochemical metamorphism. Therefore, the above results suggest that the geochemical data of the metamorphic rocks from the Changyi BIF deposit can be used to reconstruct their protoliths.

6.1.2. Protolith interpretation

Geochemical comparisons between metamorphosed and unmetamorphosed samples of different rock types have been made in numerous literatures, and thus a great number of methods, especially diagrams, were proposed to discriminate the protoliths of different types of metamorphic rocks on the basis of geochemical analyses and mineral modes (e.g., Moine and de La Roche, 1968; Simonen, 1953; Winkler, 1976). The diagram of (al + fm)-(c + alk) vs. Si is commonly used to distinguish igneous and sedimentary rocks suffered different grades of metamorphism (e.g., Meng et al., 2013; Simonen, 1953). In this diagram, the samples of the garnet-bearing gneisses mainly plot in the pelitic field, whereas the amphibolites plot in or around the area of volcanic rock (Fig. 8a). The plagioclase gneisses and leptynites, however, are much more complex. The samples scatter in the sandy and volcanic fields, and especially show trends from volcanic to pelitic rocks as well as from sandy to pelitic rocks (Fig. 8a), indicating hybrid origins. Notably, one sample (CY2-01) falling into the volcanic field also has wide range of detrital zircon U–Pb ages, which suggests that this sample is a para-metamorphic rock instead of a meta-igneous rock. The volcanic features of the samples likewise may have been related to the poor sorting of the sediments sourced from igneous rocks. The (Ca + Mg) vs. (Al + Ti + Fe) diagram was mainly proposed to distinguish metamorphosed graywackes, mafic volcanics and calcareous graywackes (Moine and de La Roche, 1968), which has been proved effectively in identifying the protoliths of amphibolites (e.g., Liègeois and Duchesne, 1981; McElhaney and McSween, 1983; Moine and de La Roche, 1968). In this diagram, all the samples of the amphibolites fall into the volcanic field (Fig. 8b), suggesting their volcanic origin. The plagioclase gneisses and leptynites plot in the fields of graywacke to subgraywacke (Fig. 8b). Diagram of ACF-A′KF has long been used in metamorphic petrology (e.g., Cornell et al., 1996; Winkler, 1976). In this diagram, the samples of the garnet-bearing gneisses show the trend from pelite to graywacke, whereas the plagioclase gneisses and leptynites mainly plot in the graywacke field and the amphibolites fall in the fields of basalt-andesite (Fig. 8c). Based on this diagram, it can be inferred that the protoliths of the garnet-bearing gneisses are pelites coupled with some contribution of detrital materials, the amphibolites are mafic volcanics and the plagioclase gneisses and leptynites are mainly graywackes. It is noteworthy that none of the samples fall into the fields of calc-silicate, ultra-basalt and granitoids, which preclude the presence of carbonate units, ultramafic and acidic volcanics during the deposition of the Changyi BIF. The ACF-A′KF diagram generally shows accordant results to those of the (al + fm)-(c + alk) vs. Si and (Ca + Mg) vs. (Al + Ti + Fe) diagrams, suggesting that the protoliths of the three types of metamorphic rocks can be reliably deduced based on the above discriminating diagrams. As a result, the protoliths of the amphibolites should be mafic volcanics, whereas the garnet-bearing gneisses should be pelites, although contaminated by clastics more or less. The protoliths of the plagioclase gneisses and leptynites should be graywackes with some contribution of pelitic materials. Diagram of $\log(SiO_2/Al_2O_3)$ vs. $\log(TFe_2O_3/K_2O)$ (Herron, 1988) can provide more specific information in identifying different kinds of sediments. According to the diagram, the protoliths of the garnet-bearing gneisses are Fe-shales (Fig. 8d). The plagioclase gneisses and leptynites, however, show multiple constituents (Fig. 8d), which are consistent with the chemical diversity of graywackes. The above inferences are supported by the mineral associations of these metamorphic rocks. In the garnet-bearing gneisses, the presence of almandine suggests Fe- and Al-rich protoliths which are accordant to Fe-rich pelites. The dominant minerals of ferrohornblende to magnesiohornblende in the amphibolites indicate Mg- and Fe-rich protoliths, consistent with mafic rocks.

6.2. Sources of the protoliths

6.2.1. Para-metamorphic rocks

Protolith reconstruction suggests that the plagioclase gneisses and leptynites as well as the garnet-bearing gneisses are meta-sedimentary rocks. Provenance of these meta-sedimentary rocks can be deduced through geochemical approaches (Mclennan et al., 1993). Since La and Th are more abundant in felsic rocks while Sc is more concentrated in mafic rocks (Taylor and McLennan, 1985; Wronkiewicz

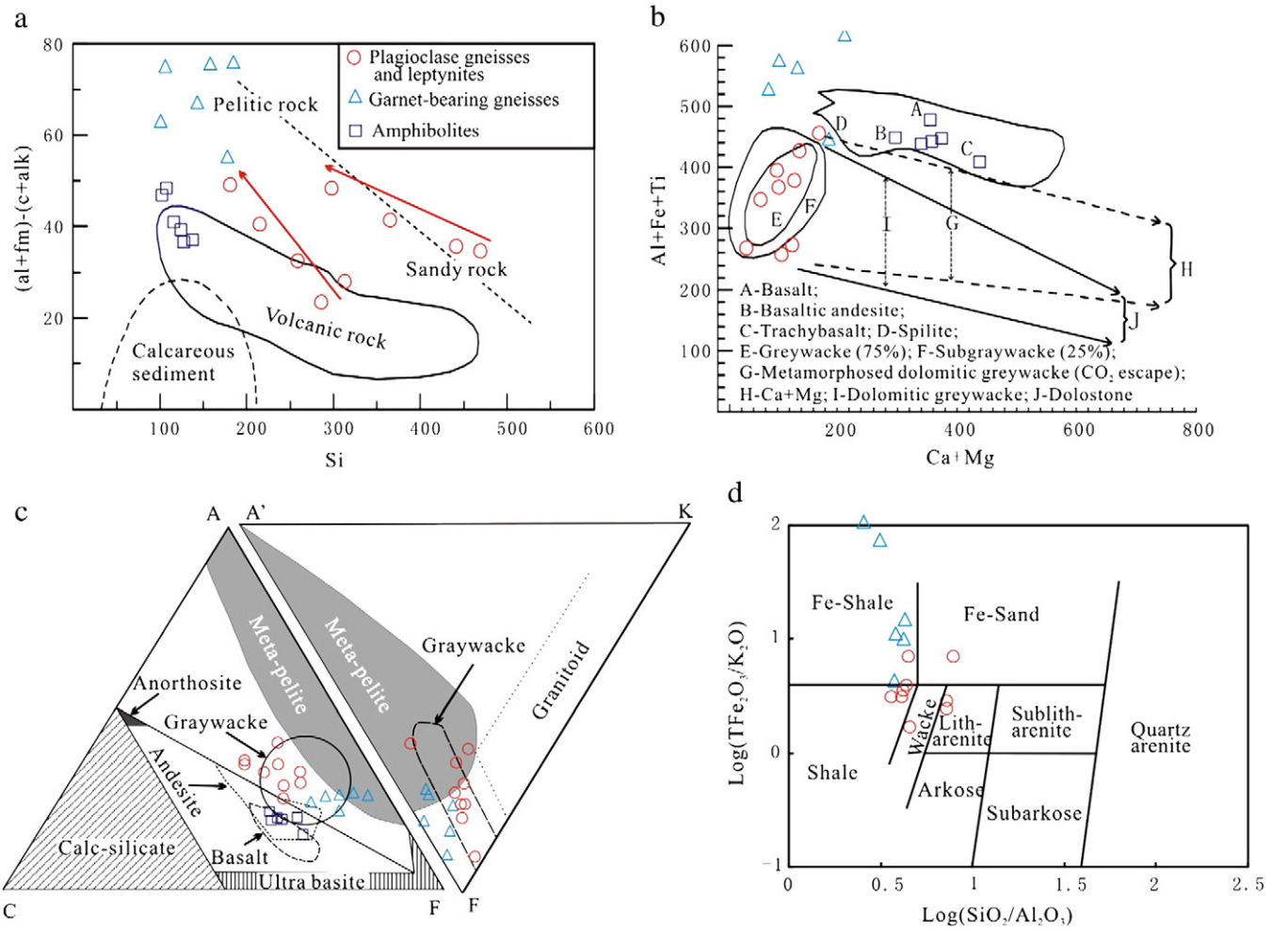

Fig. 8. Diagrams of (al + fm)-(c + alk) vs. Si (a), (Ca + Mg) vs. (Al + Ti + Fe) (b), ACF-A′KF (c) and $\log(SiO_2/Al_2O_3)$ vs. $\log(TFe_2O_3/K_2O)$ (d) discriminating the protoliths of metamorphic rocks. (a), (b), (c) and (d) are modified after Simonen (1953), Moine and de La Roche (1968), Winkler (1976), and Herron (988), respectively.

and Condie, 1987), the concentration and corresponding ratios of these elements are useful for differentiating between felsic and mafic source components (Nyakairu and Koeberl, 2001). Based on the Th vs. Sc (Fig. 9a) and La-Th-Sc (Fig. 9b) diagrams, the garnet-bearing gneisses show more involvement of mafic materials, whereas the plagioclase gneisses and leptynites have multiple source components, which were probably mainly derived from felsic rocks with some contribution of mafic materials. In addition, the source materials of the plagioclase gneisses and leptynites may have experienced sedimentary sorting and recycling, as indicated by their Zr and Hf enrichment (Fig. 6) as well as the Zr/Sc vs. Th/Sc diagram (Fig. 9c). These meta-sedimentary rocks show positive to only slightly negative Eu anomalies (δEu = 0.8–1.37, except for one sample showing 0.56), which are different from those of the post-Archean sediments but similar to the Archean rocks (Mclennan et al., 1993), suggesting that the source materials may have originated from Archean rocks. In the La vs. Th diagram, the samples of these meta-sedimentary rocks are mostly constrained to the field of Archean sediments (Fig. 9d), which confirm their provenance mainly derived from the Archean rocks. This inference is directly supported by the detrital zircons. Detrital zircons from four samples (CY2-01, CY2-40, CY2-65, CY2-83) of these meta-sedimentary rocks show $^{207}Pb/^{206}Pb$ ages of 2240–3033 Ma with concentration at 2.7–3.0 Ga (Table 1), indicating that Archean rocks are the main sources, although minor Paleoproterozoic zircons (2240 to 2246 Ma) also suggest the involvement of Paleoproterozoic materials. The detrital zircons aged by 2.7–3.0 Ga have $\varepsilon_{Hf}(t)$ values changing from −0.7 to 7.6 and mainly fall between the 3.0 Ga and 3.3 Ga average crustal evolution lines on the Age vs. $\varepsilon_{Hf}(t)$ diagram (Fig. 10), further indicating that the rocks providing materials for the meta-sedimentary rocks mainly originated from partial melting of a Mesoarchean crust. The crust-like trace element distribution patterns (strong Nb, Ta, P and Ti depletion and Pb enrichment, Fig. 6) and ancient Nd depleted mantle model ages (T_{DM} = 2.9–3.4 Ga, Table 4) of these rocks confirm their derivation from the Mesoarchean crust. However, the remarkably high $\varepsilon_{Hf}(t)$ values (from 7.5 to 9.3, Fig. 10 and Table 5) of the Paleoproterozoic detrital zircons also require minor depleted mantle-derived materials to participate in the deposition of the meta-sedimentary rocks.

6.2.2. Ortho-metamorphic rocks

Almost all the discriminating diagrams show that the amphibolites from the Changyi BIF deposit are meta-volcanics. The widespread amphibolites interbedded with the BIF bands therefore suggest extensive volcanic activity during the BIF deposition. The amphibolites are characterized by low SiO_2 (46.5 to 52.8 wt.%) and high MgO (5.68 to 10.9 wt.%) contents, which indicate that the protoliths of these amphibolites are probably mafic volcanics. In the TAS diagram, the samples of the amphibolites plot in the fields of basalt and basaltic andesite (Fig. 11a). Immobile elements such as Ti, Zr, Y and Nb are more reliable than the major elements when applied to meta-volcanic rocks as these elements can keep stable during post-consolidation alteration and metamorphic processes (Floyd and Winchester, 1978; Winchester and Floyd, 1976). In the Nb/Y vs. Zr/Ti discriminating diagram (Fig. 11b), the amphibolite samples are also classified as basalt to basaltic andesite, which not only support the result of the TAS diagram, but also further

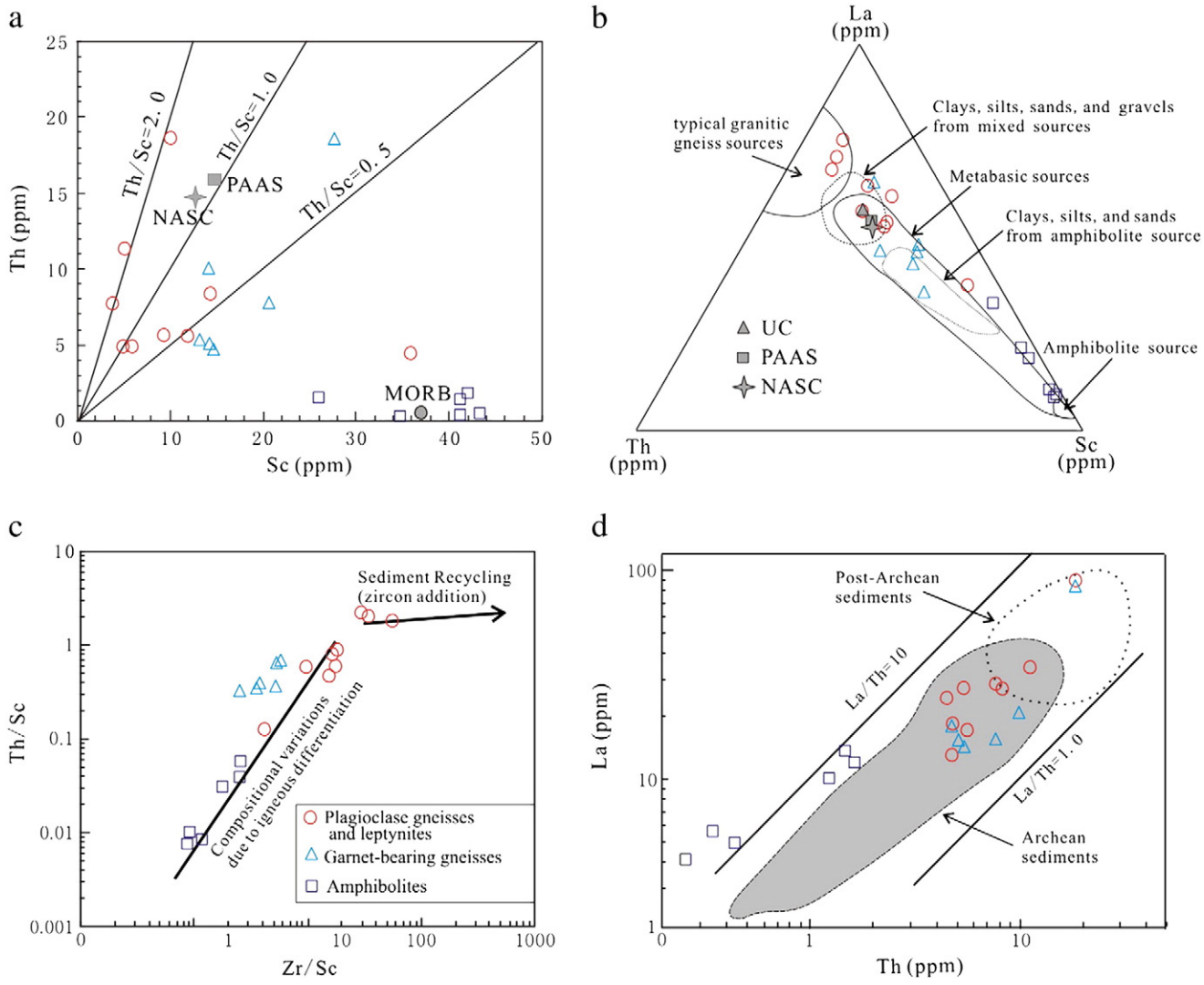

Fig. 9. Diagrams of Th vs. Sc (a), La-Th-Sc (b), Th/Sc vs. Zr/Sc (c) and La vs. Th (d) for discriminating the provenance of the meta-sedimentary rocks. Post-Archean Australian Shale (PAAS, McLennan, 1989), North American Shale Composite (NASC, Gromet et al., 1984) and upper continental cust (UC, Taylor and McLennan, 1985) are shown for comparion in (a) and (b). (b), (c) and (d) are after Cullers (1994), McLennan et al. (1993) and McLennan (1989), respectively.

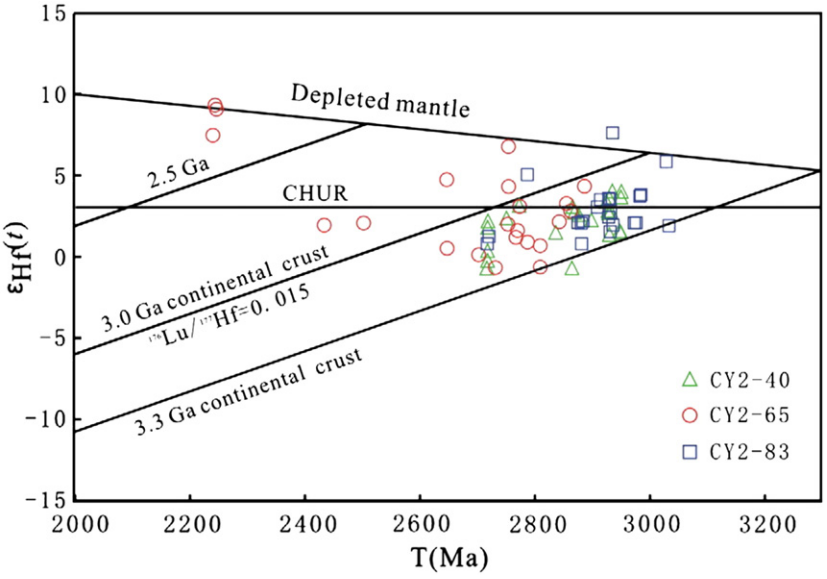

Fig. 10. Diagram of Hf isotopic evolution in zircons from the para-metamorphic rocks.

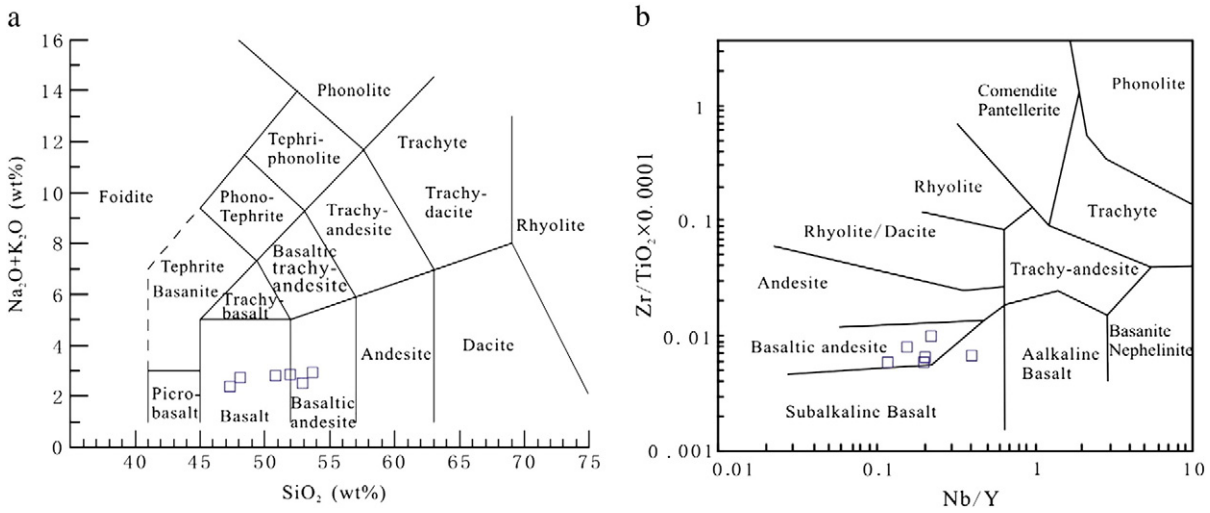

Fig. 11. Diagrams of ($Na_2O + K_2O$) vs. SiO_2 (TAS) (a) and Zr/TiO_2 vs. Nb/Y (b) for volcanic rocks nomenclature. (a) and (b) are after Le Bas et al. (1986) and Winchester and Floyd (1976), respectively.

prove that the amphibolites have not suffered significant major elements loss during the amphibolite facies metamorphism. The low $K_2O + Na_2O$ contents (2.52 to 3.06 wt.%) indicate that these meta-volcanics belong to subalkaline series (Fig. 12a, b). In addition, the relatively low Al_2O_3 contents (12.0 to 15.1 wt.%) classify these rocks into tholeiitic rocks (Fig. 12c,d).

Tholeiites can occur in various tectonic settings, such as mid-oceanic ridge, oceanic island, island arc and continental rift. Compared with tholeiites produced in different tectonic settings, the major elements of the meta-tholeiites from the Changyi BIF deposit show more affinities to those of the continental tholeiites (Fig. 13). However, the distinct depletion of Nb, Ta, P and Ti and enrichment of Pb of these meta-tholeiites are similar to those of the island arc tholeiites or the continental crust (Fig. 6e, f), indicating that these rocks may have been produced in island arc or contaminated by crustal materials within continent. Former studies have proved that contamination by continental crust can impart

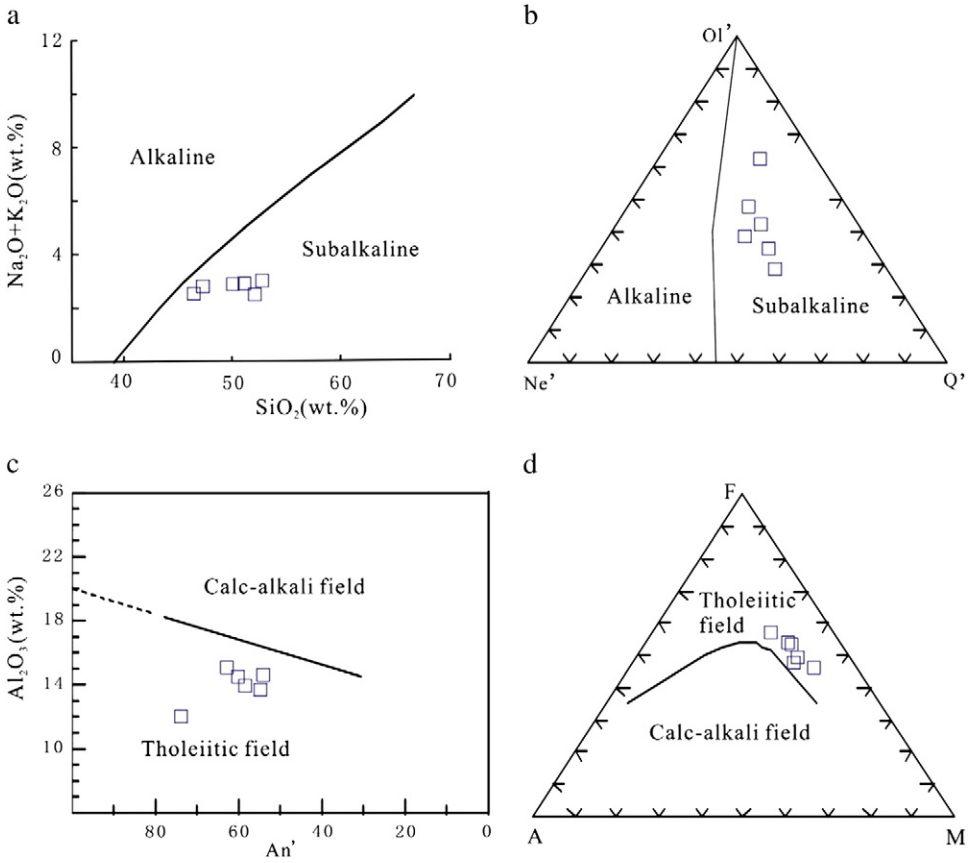

Fig. 12. Diagrams of SiO_2 vs. $K_2O + Na_2O$ (a), Ol′-Ne′-Q′ (b), An′ vs. Al_2O_3 (c) and AFM (d) dividing the basalts into different suites. All the diagrams are from Irvine and Baragar (1971). Ol′, Ne′, Q′ and An′ are calculated by using the cation norm, Ol′ = Ol + 3/4Opx, Ne′ = Ne + 3/5Ab, Q′ = Q + 2/5Ab + 1/4Opx, An′ = 100An/(An + Ab + 5/3Ne). F = FeO + 0.8998Fe_2O_3, A = $K_2O + Na_2O$, M = MgO, all in weight percent.

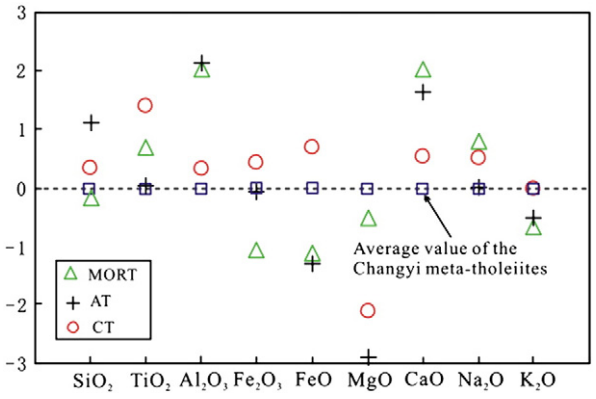

Fig. 13. Comparison of average major elements compositions between the Changyi meta-tholeiites and other tholeiites in different tectonic settings. The data of CT, AT and MORT are from Condie (1976). CT—continental tholeiite; AT—arc tholeiite; MORT—mid-ocean ridge tholeiite.

subduction-type signatures and lead to the misidentification of basalts as arc related (Ernst et al., 2005; Xia et al., 2007). Coupled with Nb, Ta and Ti depletion, high $(Th/Nb)_N$ (>1) and La/Nb ratios (>1) and low $\varepsilon_{Nd}(t)$ value (<0) were considered as the typical features of the continental basalts contaminated by crustal materials (e.g., Kieffer et al., 2004; Saunders et al., 1992; Xia et al., 2004, 2007). The meta-tholeiites in this study have obviously high $(Th/Nb)_N$ (0.90 to 3.00) and Nb/La ratios (1.72 to 2.86) and low $\varepsilon_{Nd}(t)$ values (−4.4 to −0.2), suggesting that these meta-tholeiites were likely contaminated by continental crust. In addition, the $\varepsilon_{Nd}(t)$ values of the meta-tholeiites generally show negative and positive correlation with the whole-rock SiO_2 and MgO contents, respectively (Fig. 14a, b), also providing evidence for continental crustal contamination. The low initial Sr isotopic compositions ($^{87}Sr/^{86}Sr_i$ = 0.703127–0.705597) of these rocks (Table 4) suggest that the crustal materials could be mainly derived from lower crust instead of upper crust. In addition, the ancient Nd depleted mantle model ages (T_{DM} = 3.0–3.4 Ga) require Mesoarchean crustal materials for contamination. The least contaminated sample has $\varepsilon_{Nd}(t)$ values comparable to those of the Paleoproterozoic mafic dykes derived from subcontinental lithospheric mantle (t = −2147 Ma, $\varepsilon_{Nd}(t)$ = −3.2–3, Peng et al., 2012), suggesting that these meta-tholeiites may have also originated from partial melting of such subcontinental lithospheric mantle during Paleoproterozoic.

6.3. Depositional environment

The REE distribution patterns of the Changyi BIF show LREE depletion, positive La and Y anomalies, and superchondritic Y/Ho ratios (26.8 to 48.1) (Lan et al., 2013), which are also the common features of seawater (e.g., Alibo and Nozaki, 1999; Bolhar et al., 2004; Freslon et al., 2011; Nozaki et al., 1997; Sholkovitz et al., 1994; Zhang and Nozaki, 1996), suggesting that the BIF bands and their wallrocks occurred in seawater. Cross-bedding and lens-shaped BIF bands are observed in the Changyi BIF, which could not be produced by deuteric diagenesis and metamorphism due to their weak deformation and the conformable contact with their wallrocks (Lan et al., 2013). Therefore, these structures should be originally depositional structures produced by waves, indicating that the BIF bands and their meta-sedimentary wallrocks were originally deposited in a high-energy environment, possibly above wave base. Actually, the abundant Archean crustal materials involved in the Paleoproterozoic sedimentation also support a nearshore depositional basin. Therefore, the shallow depositional environment suggests that the Changyi BIF may have certain affinities to the GIFs that are typically associated with shallow-water, high-energy environment (Trendall, 2002).

Depositional basins in different tectonic settings, such as intra-arc or back-arc basins in island arc settings (e.g., Basta et al., 2011; González et al., 2009; Polat and Frei, 2005; Zhang et al., 2011b; Zhang et al., 2012b), oceanic basins near mid-ocean ridges (e.g., Kato et al., 1998; Khan et al., 1996), rift basins (e.g., Bekker et al., 2010; Breitkopf, 1988; Hatton and Davidson, 2004) and epicontinental basins (e.g., Beukes and Gutzmer, 2008; Klemm, 2000), have been invoked to explain the deposition of IFs. For the Changyi BIF, the widespread meta-tholeiites produced within ancient continent suggest an intra-continental environment for the deposition of the BIF. In addition, the Paleoproterozoic alkaline granites (2169 to 2193 Ma) intruding the Changyi BIF are characterized by A-type granite features and show Mesoarchean T_{DM} ages (2809 to 2868 Ma) (our unpublished data), strongly supporting a rift within an ancient continent. A continental rift setting was also proposed in a recent work on the Paleoproterozoic magmatic belts in the NCC (Peng et al., 2012). Furthermore, the Fenzishan group hosting the Changyi BIF has long been considered to form in a continental rift (e.g., Wang et al., 2009; Yu, 1996; Zhai and Peng, 2007; Zhai and Santosh, 2011; Zhao et al., 2005). Since seawater is required for the BIF deposition, an intra-continental rift, which should have been opened to the ocean, is therefore proposed for the formation of the Changyi BIF and its wallrocks (Fig. 15).

6.4. Tectonic implications

Two contrasting models about the Paleoproterozoic evolution of the eastern NCC have been hotly debated during recent years. One considers that this area experienced opening and closing of a continental rift (Li et al., 2005, 2011; Li and Zhao, 2007; Peng and Palmer, 1995; Yu, 1996; Zhao et al., 2005), whereas the other supports amalgamation processes between independent continental terranes (He and Ye, 1998; Faure et al., 2004; Lu et al., 2006; Meng et al., 2013). Bimodal volcanic

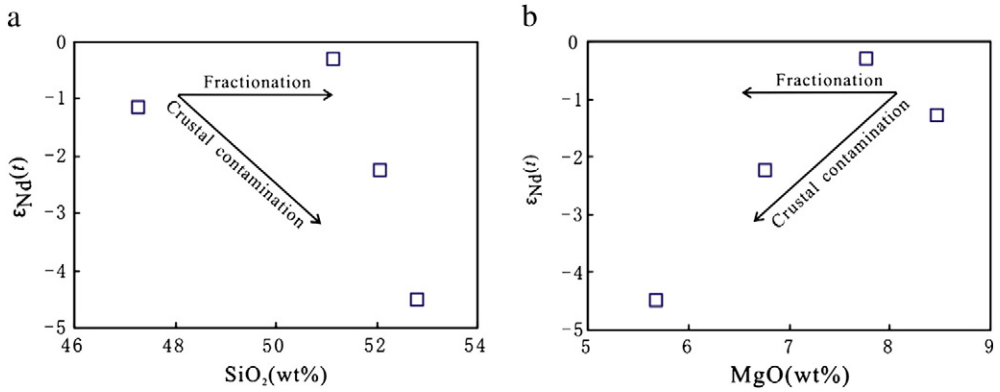

Fig. 14. Plots of $\varepsilon_{Nd}(t)$ vs. SiO_2 (a) and $\varepsilon_{Nd}(t)$ vs. MgO (b) for the meta-tholeiites from the Changyi BIF area.

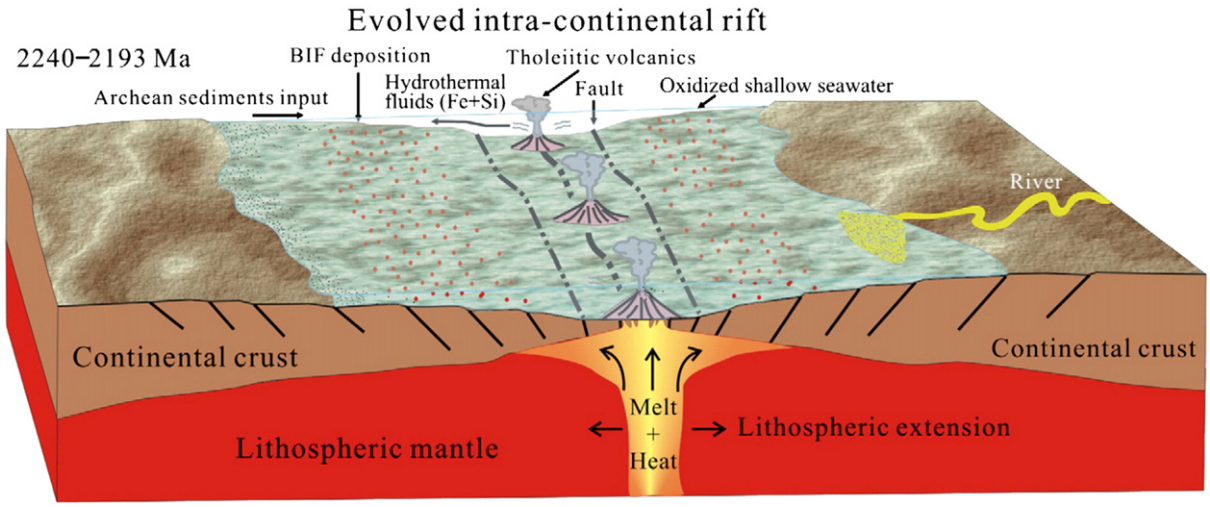

Fig. 15. Tectonic model for the formation of the Changyi BIF and its wallrocks (modified after Lan et al., 2013).

rocks (Peng and Palmer, 1995; Sun et al., 1996; Yu, 1996; Zhang and Yang, 1988), A-type granites (Chen et al., 2001; Li et al., 2004; Li and Yang, 1997; Zhang and Yang, 1988), anticlockwise P–T paths (Dong and Wang, 1998; Li et al., 2001; Lu, 1996) and non-marine borate-bearing sedimentary successions (Peng and Palmer, 1995, 2002) are considered as the robust evidence for a Paleoproterozoic continental rift. In contrast, sediments with active continental margin signatures (e.g., Meng et al., 2013) and clockwise *P–T–t* paths (He and Ye, 1998; Wang et al., 2010; Zhou et al., 2007) were also observed in the Paleoproterozoic successions, which support the subduction–collision processes between independent continental terranes. In the Changyi BIF deposit, continental tholeiites and A-type granites are recognized, supporting a tectonic setting of continental rift instead of an active continental margin. This area may have kept largely stable during ca. 2.3–2.5 Ga and not been disturbed until ca. 2.2–2.3 Ga, as suggested by the lack of 2.3–2.5 Ga detrital zircons and the appearance of mantle-derived ~2.2 Ga zircons in the meta-sedimentary rocks. Amphibolite facies metamorphism occurring at ~1860 Ma is recorded by the Changyi BIF (Lan et al., 2012, 2013), which is well in accord with the Paleoproterozoic collisional events associated with the final cratonization of the NCC (Zhai and Santosh, 2011; Zheng et al., 2012). Therefore, the formation of the Changyi BIF and its wallrocks witnessed the Paleoproterozoic rifting-collision events in the eastern NCC.

This unique tectonic environment may have been responsible for the contrasting distribution features between the Archean and Paleoproterozoic BIFs in the NCC. In the central and eastern NCC, Archean BIFs are widespread in Shanxi, Hebei, Liaoning and western Shandong Provinces (Shen et al., 2005; Zhang et al., 2012a), whereas the Paleoproterozoic BIFs are sporadically distributed in the Lvliang area of Shanxi Province (Li et al., 2010), Dalizi area of Jilin Province (Zhai, 2010; Zhai and Shen, 1994; Zhang, 1988) and Changyi area of eastern Shandong Province (Lan et al., 2012; Wang et al., 2007; Xu et al., 2011). Previous studies reported that the Archean BIFs in the NCC mainly belong to Algoma-type and were commonly produced in island arc settings (Zhai, 2010; Zhang et al., 2011b; Zhang et al., 2012a, 2012b). In contrast, the Paleoproterozoic BIFs were considered to belong to Superior-type (Shen et al., 2005; Zhai, 2010; Zhai and Shen, 1994; Zhang, 1988) and were hosted in the Paleoproterozoic sequences deposited within continental rifts (Wang et al., 2009; Yu, 1996; Zhai and Peng, 2007; Zhai and Santosh, 2011; Zhao et al., 2005). Thus, the tectonic settings may have played an important role in controlling the nature and distribution of the Archean and Paleoproterozoic BIFs. At least seven Archean micro-blocks have been identified in the NCC (Zhai and Santosh, 2011), the amalgamation of which was accompanied by generation of intense magmatic activities and arc-related basins. These magmatic activities and depositional basins would provide favorable environments for the deposition of the Algoma-type BIFs, giving rise to the abundant Archean BIFs in the NCC. Several Neoarchean greenstone belts surrounding the micro-blocks not only represent the vestiges of older arc-continent collision (Zhai and Santosh, 2011) but also host most of the Archean Algoma-type BIFs (Zhang et al., 2012a), which prove the amalgamation processes resulting in the development of the Archean BIFs. As cratonization of the NCC was accomplished at the end of Neoarchean (about ca. 2.5 Ga) through amalgamation of these micro-blocks (Zhai and Santosh, 2011), major tectonic events did not occur until ca. 2350–1970 Ma, at which time an orogenic cycle from rifting to subduction–collision operated in the NCC (Zhai and Santosh, 2011). However, the Paleoproterozoic rifting was confined to specific regions (Fig. 1) and thus provided poor environments for the BIF deposition. The lack of depositional basins may be responsible for the scarcity of the Paleoproterozoic BIFs in the NCC.

7. Conclusions

Systematic petrological, geochronological and geochemical studies on the wallrocks from the Changyi BIF deposit lead to the following conclusions.

(1) Three major types of metamorphic wallrocks are identified, including plagioclase gneisses and leptynites, garnet-bearing gneisses and amphibolites.
(2) The protoliths of the plagioclase gneisses and leptynites are mainly graywackes with minor contribution of pelitic materials, the garnet-bearing gneisses are Fe-rich pelites contaminated by some clastics, and the amphibolites are tholeiitic rocks.
(3) The para-metamorphic rocks were mainly sourced from a Archean crust with minor involvement of Paleoproterozoic materials, whereas the ortho-metamorphic rocks mainly originated from partial melting of the subcontinental lithospheric mantle.
(4) An intra-continental rift is suggested for the deposition of the Changyi BIF. The poor depositional environment in continental rift is possibly responsible for the scarcity of the Paleoproterozoic BIFs in the NCC.

Acknowledgments

We are grateful to Chao-Feng Li for help during Sr–Nd isotopes analyses, Zhao-Chu Hu for help during zircon LA-ICP-MS U–Pb dating, Yue-Heng Yang for help during zircon Hf analyses, and He Li and

Wen-Jun Li for help during major and trace element analyses. This study was financially supported by the Major State Basic Research Development Program (2012CB416605) and the Natural Science Foundation of China (41202065).

References

Alibo, D.S., Nozaki, Y., 1999. Rare earth elements in seawater: particle association, shale normalization, and Ce oxidation. Geochim. Cosmochim. Acta 63, 363–372.

Alirezaei, S., Cameron, E.M., 2002. Mass balance during gabbro-amphibolite transition, Bamble Sector, Norway: implications for petrogenesis and tectonic setting of the gabbros. Lithos 60, 21–45.

Barth, M.G., McDonough, W.F., Rudnick, R.L., 2000. Tracking the budget of Nb and Ta in the continental crust. Chemical Geology 165, 197–213.

Basta, F.F., Maurice, A.E., Fontbotéc, L., Favargerd, P.Y., 2011. Petrology and geochemistry of the banded iron formation (BIF) of Wadi Karim and Um Anab, Eastern Desert, Egypt: implications for the origin of Neoproterozoic BIF. Precambrian Res. 187, 277–292.

Bauernhofer, A.H., Hauzenberger, C.A., Wallbrecher, E., Muhongo, S., Hoinkes, G., Mogessie, A., Opiyo-Akech, N., Tenczer, V., 2009. Geochemistry of basement rocks from SE Kenya and NE Tanzania: indications for rifting and early Pan-African subduction. Int. J. Earth Sci. 98, 1809–1834.

Bekker, A., Slack, J.F., Planavsky, N., Krapez, B., Hofmann, A., Konhauser, K.O., Rouxel, O.J., 2010. Iron formation: the sedimentary product of a complex interplay among mantle, tectonic, oceanic, and biospheric processes. Econ. Geol. 105, 467–508.

Beukes, N.J., Gutzmer, J., 2008. Origin and paleoenvironmental significance of major iron formations at the Archean–Paleoproterozoic boundary. Rev. Econ. Geol. 15, 5–47.

Blichert-Toft, J., Albaréde, F., 1997. The Lu–Hf isotope geochemistry of chondrites and the evolution of the mantle–crust system. Earth Planet. Sci. Lett. 148, 243–258.

Bolhar, R., Kamber, B.S., Moorbath, S., Fedo, C.M., Whitehouse, M.J., 2004. Characterization of Early Archean chemical sediments by trace element signatures. Earth Planet. Sci. Lett. 222, 43–60.

Breitkopf, J.H., 1988. Iron formations related to mafic volcanism and ensialic rifting in the southern margin zone of the Damara orogen, Namibia. Precambrian Res. 38, 111–130.

Chen, L., 2010. Concordant structural variations from the surface to the base of the upper mantle in the North China Craton and its tectonic implications. Lithos 120, 96–115.

Chen, S.L., Huan, Y.Q., Bing, Z.B., 2001. Characteristics of Palaeoproterozoic intrusive rocks and continental dynamic evolution of tectono-magmatism in the eastern Liaoning. Liaoning Geol. 18, 43–50 (in Chinese with English Abstract).

Condie, K.C., 1976. Trace element geochemistry of Archean greenstone belts. Earth Sci. Rev. 12, 393–417.

Cornell, D.H., Thomas, R.J., Bowring, S.A., Armstrong, R.A., Grantham, G.H., 1996. Protolith interpretation in metamorphic terranes: a back-arc environment with Besshi-type base metal potential for the Quha Formation, Natal Province, South Africa. Precambrian Res. 77, 243–271.

Cullers, R.L., 1994. The chemical signature of source rocks in size fractions of Holocene stream sediment derived from metamorphic rocks in the wet mountains region, Colorado, USA. Chem. Geol. 113, 327–343.

Dong, Y.S., Wang, W., 1998. The style of metamorphic evolution of early Proterozoic Jingshan Group in Eastern Shandong Province and its tectonic environment. Glob. Geol. 17, 1–8 (in Chinese with English abstract).

Drury, S.A., 1978. REE distributions in a high-grade Archaean gneiss complex in Scotland: implications for the genesis of ancient sialic crust. Precambrian Res. 7, 237–257.

Ernst, R.E., Buchan, K.L., Campbell, I.H., 2005. Frontiers in large igneous province research. Lithos 79, 271–297.

Faure, M., Lin, W., Moni, P., Bruguier, O., 2004. Paleoproterozoic arc magmatism and collision in Liaodong Peninsula, NE China. Terra Nova 16, 75–80.

Fernandes, J.F., Iyer, S.S., Imakuma, K., Choudhuri, A., 1987. Geochemical studies in the proterozoic metamorphic terrane of the guaxupé massif, minas gerais, brazil. A discussion on large ion lithophile element fractionation during high-grade metamorphism. Precambrian Res. 36, 65–79.

Floyd, P.A., Winchester, J.A., 1978. Identification and discrimination of altered and metamorphosed volcanic rocks using immobile elements. Chem. Geol. 21, 291–306.

Freslon, N., Bayon, G., Birota, D., Bollinger, C., Barrat, J.A., 2011. Determination of rare earth elements and other trace elements (Y, Mn, Co, Cr) in seawater using Tm addition and $Mg(OH)_2$ co-precipitation. Talanta 85, 582–587.

Gao, S., Rudnick, R.L., Carlson, R.W., McDonough, W.F., Liu, Y.S., 2002. Re–Os evidence for replacement of ancient mantle lithosphere beneath the North China craton. Earth Planet. Sci. Lett. 198, 307–322.

Garofalo, P.S., 2012. The composition of Alpine marine sediments (Bündnerschiefer Formation, W Alps) and the mobility of their chemical components during orogenic metamorphism. Lithos 128–131, 55–72.

González, P.D., Sato, A.M., Llambías, E.J., Petronilho, L.A., 2009. Petrology and geochemistry of the banded iron formation in the Eastern Sierras Pampeanas of San Luis (Argentina): implications for the evolution of the Nogolí Metamorphic Complex. J. S. Am. Earth Sci. 28, 89–112.

Goolaerts, A., Mattielli, N., Jong, J.D., Weis, D., Scoatea, J.S., 2004. Hf and Lu isotopic reference values for the zircon standard 91500 by MC-ICP-MS. Chem. Geol. 206, 1–9.

Green, T.H., Brunfelt, A.O., Heier, K.S., 1972. Rare-earth element distribution and K/Rb ratios in granulites, mangerites and anorthosites, Lofoten-Vesteraalen, Norway. Geochim. Cosmochim. Acta 36, 241–257.

Griffin, W.L., Zhang, A.D., O'Reilly, S.Y., Ryan, C.G., 1998. Phanerozoic evolution of the lithosphere beneath the Sino-Korean Craton. In: Flower, M.F.J., Chung, S.L., Lo, C.H., Lee, T.Y. (Eds.), Mantle dynamics and plate interactions in East Asia. American Geophysical Union–Geodynamics Series, 27, pp. 107–126.

Griffin, W.L., Pearson, N.J., Belousova, E., Jackson, S.E., Achterbergh, E.V., O'Reilly, S.Y., Shee, S.R., 2000. The Hf isotope composition of cratonic mantle: LAM-MC-ICPMS analysis of zircon megacrysts in kimberlites. Geochim. Cosmochim. Acta 64, 133–147.

Gromet, L.P., Dymek, R.F., Haskin, L.A., Korotev, R.L., 1984. The 'North American Shale Composite': its compilation, major and trace element characteristics. Geochim. Cosmochim. Acta 48, 2469–2482.

Gross, G.A., 1980. A classification of iron formations based on depositional environments. Can. Mineral. 18, 215–222.

Gross, G.A., 1983. Tectonic systems and the deposition of iron-formation. Precambrian Res. 20, 171–187.

Hatton, O.J., Davidson, G.J., 2004. Soldiers Cap Group iron-formations, Mt. Isa inlier, Australia, as windows into the hydrothermal evolution of a base-metal-bearing Proterozoic rift basin. Aust. J. Earth Sci. 51, 85–106.

He, G.P., Ye, H.W., 1998. Two type of Early Proterozoic metamorphism in the eastern Liaoning to southern Jilin and their tectonic implication. Acta Petrol. Sin. 14, 152–162 (in Chinese with English abstract).

Herron, M.M., 1988. Geochemical classification of terrigenous sands and shales from core or log data. J. Sediment. Petrol. 58, 820–829.

Huston, D.L., Logan, G.A., 2004. Barite, BIFs and bugs: evidence for the evolution of the Earth's early hydrosphere. Earth Planet. Sci. Lett. 220, 41–55.

Irvine, T.N., Baragar, W.R.A., 1971. A guide to the chemical classification of the common volcanic rocks. Can. J. Earth Sci. 8, 523–548.

Jahn, B.M., Zhang, Z.Q., 1984. Archean granulite gneisses from eastern Hebei Province, China: rare earth geochemistry and tectonic implications. Contrib. Mineral. Petrol. 85, 224–243.

Jahn, B.M., Liu, D.Y., Wan, Y.S., Song, B., Wu, J.S., 2008. Archean crustal evolution of the Jiaodong peninsula, China, as revealed by zircon SHRIMP geochronology, elemental and Nd-isotope geochemistry. Am. J. Sci. 308, 232–269.

Kamber, B.S., Collerson, K.D., 2000. Role of 'hidden' deeply subducted slabs in mantle depletion. Chem. Geol. 166, 241–254.

Kato, Y., Ohta, I., Tsunematsu, T., Watanabe, Y., Isozaki, Y., Maruyama, S., Imai, N., 1998. Rare earth element variations in mid-Archean banded iron formations: implications for the chemistry of ocean and continent and plate tectonics. Geochim. Cosmochim. Acta 62, 3475–3497.

Kelemen, P.B., Hanghøj, K., Greene, A.R., 2007. 3.18-One view of the geochemistry of subduction-related magmatic arcs, with an emphasis on primitive andesite and lower crust. Treatise on Geochemistry, pp. 1–70.

Khan, R.M.K., Das Sharma, S., Patil, D.J., Naqvi, S.M., 1996. Trace, rare-earth element, and oxygen isotopic systematics for the genesis of banded iron-formations: evidence from Kushtagi schist belt, Archaean Dharwar Craton, India. Geochim. Cosmochim. Acta 60, 3285–3294.

Kieffer, B., Arndt, N., Lapierre, H., et al., 2004. Flood and shield basalts from Ethiopia: magmas from the African Superswell. J. Petrol. 45, 793–834.

Klemm, D.D., 2000. The formation of Palæoproterozoic banded iron formations and their associated Fe and Mn deposits, with reference to the Griqualand West deposits, South Africa. J. Afr. Earth Sci. 30, 1–24.

Lan, T.G., Fan, H.R., Hu, F.F., Yang, K.F., Zheng, X.L., Zhang, H.D., 2012. Geological and geochemical characteristics of Paleoproterozoic Changyi banded iron formation deposit, Jiaodong Peninsula of eastern China. Acta Petrol. Sin. 28, 3595–3611 (in Chinese with English abstract).

Lan, T.G., Fan, H.R., Santosh, M., Hu, F.F., Yang, K.F., Yang, Y.H., Liu, Y.S., 2013. U–Pb zircon chronology, geochemistry and isotopes of the Changyi banded iron formation in eastern Shandong Province: constraints on BIF genesis and implications for Paleoproterozoic tectonic evolution of the North China Craton. Ore Geol. Rev 56, 472–486.

Le Bas, M.J., LeMaitre, R.W., Streckeisen, A., Zanettin, B., IUGS Subcommission on the Systematics of Igneous Rocks, 1986. A chemical classification of volcanic rocks based on the total alkali-silica diagram. J. Petrol. 27, 745–750.

Li, S.Z., Yang, Z.S., 1997. Types and genesis of palaeoproterozoic granites in the Jiao-Liao Massif. Northwest. Geol. 43, 21–27 (in Chinese with English abstract).

Li, S.Z., Zhao, G.C., 2007. SHRIMP U–Pb zircon geochronology of the Liaqji granitoids: constraints on the evolution of the Paleoproterozoic Jiao-Liao-Ji belt in the eastern block of the North China craton. Precambrian Res. 158, 1–16.

Li, S.Z., Han, Z.Z., Liu, Y.J., Yang, Z.S., Ma, R., 2001. Continental dynamics and regional metamorphism in the Liaohe Group. Geol. Rev. 47, 9–18 (in Chinese with English abstract).

Li, S.Z., Zhao, G.C., Sun, M., Liu, J.Z., Hao, D.F., Han, Z.Z., Luo, Y., Yang, Z.Z., 2004. Not all the Liaoji Granitoids are Paleoproterozoic: evidence from SHRIMP U–Pb zircon ages. Int. Geol. Rev. 46, 162–176.

Li, S.Z., Zhao, G.C., Sun, M., Wu, F.Y., Hao, D.F., Han, Z.Z., Luo, Y., Xia, X.P., 2005. Deformational history of the Paleoproterozoic Liaohe Group in the Eastern Block of the North China Craton. J. Asian Earth Sci. 24, 659–674.

Li, Z.H., Zhu, X.K., Tang, S.H., Li, J., Liu, H., 2010. Characteristics of rare earth elements and geological significations of BIFs from Jidong, Wutai and Lüliang area. Geoscience 24, 840–846 (in Chinese with English abstract).

Li, S.Z., Zhao, G.C., Santosh, M., Liu, X., Dai, L.M., 2011. PPalaeoproterozoic tectonothermal evolution and deep crustal processes in the Jiao-Liao-Ji Belt, North China Craton: a review. Geol. J. 46, 525–543.

Liègeois, J., Duchesne, J., 1981. The Lac Cornu retrograded eclogites (Aigailles Rouges massif, Western Alps France): evidence of crustal origin and metasomafic alteration. Lithos 14, 35–48.

Liu, Y.S., Hu, Z.C., Gao, S., Günther, D., Xu, J., Gao, C.G., Chen, H.H., 2008. In situ analysis of major and trace elements of anhydrous minerals by LA-ICP-MS without applying an internal standard. Chem. Geol. 257, 34–43.

Lu, L.Z., 1996. The Precambrian metamorphic geology and tectonic evolution of the Jiao-Liao massif. J. Changchun Univ. Earth Sci. 26, 25–32 (in Chinese with English abstract).
Lu, X.P., Wu, F.Y., Guo, J.H., Wilde, S.A., Yang, J.H., Liu, X.M., Zhang, X.O., 2006. Zircon U–Pb geochronological constraints on the Paleoproterozoic crustal evolution of the Eastern block in the North China Craton. Precambrian Res. 146, 138–164.
Ludwig, K.R., 2003. User's Manual for Isoplot 3.00, a geolocronolgical Toolkit for Microsoft Excel. Berkeley Geochronlogical Center Special Publication, No. 4, pp. 25–32.
Lugmair, G.W., Harti, K., 1978. Lunar initial $^{143}Nd/^{144}Nd$: differential evolution of the lunar crust andMantle. Earth Planet. Sci. Lett. 39, 349–357.
McElhaney, M.S., McSween Jr., H.Y., 1983. Petrology of the Chunky Gal Mountain mafic–ultramafic complex, North Carolina. Geol. Soc. Am. Bull. 94, 855–874.
McLennan, S.M., 1989. Rare earth elements in sedimentary rocks; influence of provenance and sedimentary processes. Rev. Mineral. Geochem. 21, 169–200.
McLennan, S.M., Hemming, S., McDaniel, D.K., Hanson, G.N., 1993. Geochemical approaches to sedimentation, provenance and tectonics. Geol. Soc. Am. Spec. Pap. 284, 21–40.
Meng, E., Liu, F.L., Cui, Y., Cai, J., 2013. Zircon U–Pb and Lu–Hf isotopic and whole-rock geochemical constraints on the protolith and tectonic history of the Changhai metamorphic supracrustal sequence in the Jiao–Liao–Ji Belt, southeast Liaoning Province, northeast China. Precambrian Res. 233, 297–315.
Menzies, M.A., Xu, Y.G., 1998. Geodynamics of the North China Craton. In: Flower, M.F.J., Chung, S.L., Lo, C.H., Lee, T.Y. (Eds.), Mantle Dynamics and Plate Interactions in East Asia. American Geophysical Union–Geodynamics Series, 27, pp. 155–165.
Moine, B., de La Roche, H., 1968. Nouvelle approche du problème de l'origine des amphibolites à partir de leur composition chimique. Acad. Sci. Paris C.R. 267, 2084–2087.
Nozaki, Y., Zhang, J., Amakawa, H., 1997. The fractionation between Y and Ho in the marine environment. Earth Planet. Sci. Lett. 148, 329–340.
Nyakairu, G.A.W., Koeberl, C., 2001. Mineralogical and chemical composition and distribution of rare earth elements in clay-rich sediments from central Uganda. Geochem. J. 35, 13–28.
Pearce, J.A., Norry, M.J., 1979. Petrogenetic implications of Ti, Zr, Y, and Nb variations in volcanic rocks. Contrib. Mineral. Petrol. 69, 33–47.
Peng, Q.M., Palmer, M.R., 1995. The Palaeoproterozoic boron deposits in eastern Liaoning, China: a metamorphosed evaporite. Precambrian Res. 72, 185–197.
Peng, Q.M., Palmer, M.R., 2002. The Paleoproterozoic Mg and Mg–Fe borate deposits of Liaoning and Jilin Provinces, northeast China. Econ. Geol. 97, 93–108.
Peng, P., Guo, J.H., Zhai, M.G., Windley, B.F., Li, T.S., Liu, F., 2012. Genesis of the Hengling magmatic belt in the North China Craton: implications for Paleoproterozoic tectonics. Lithos 148, 27–44.
Polat, A., Frei, R., 2005. The origin of early Archean banded iron formations and of continental crust, Isua, southern West Greenland. Precambrian Res. 138, 151–175.
Rudnick, R.L., Gao, S., 2003. Composition of the continental crust. Treatise on Geochemistry, 3, pp. 1–64.
Rudnick, R.L., McLennan, S.M., Taylor, S.R., 1985. Large ion lithophile elements in rocks from high-pressure granulite facies terrains. Geochim. Cosmochim. Acta 49, 1645–1655.
Saunders, A.D., Storey, M., Kent, R.W., Norry, M.J., 1992. Consequences of plume–lithosphere interaction. Geol. Soc. Lond. Spec. Publ. 68, 41–60.
Schüssler, U., Richter, P., Okrusch, M., 1989. Metabasites from the KTB target area Oberpfalz—geochemical characteristics and examples for mobile behaviour of "immobile" elements. Tectonophysics 157, 135–148.
Shaw, D.M., 1968. A review of K–Rb fractionation trends by covariance analysis. Geochim. Cosmochim. Acta 32, 573–602.
Shen, B.F., Zhai, A.M., Yang, C.L., Cao, X.L., 2005. Temporal–spatial distribution and evolutional characters of Precambrian iron deposits in China. Geol. Surv. Res. 28, 196–206 (in Chinese with English abstract).
Sholkovitz, E.R., Landing, W.M., Lewis, B.L., 1994. Ocean particle chemistry: the fractionation of rare earth elements between suspended particles and seawater. Geochim. Cosmochim. Acta 58, 1567–1579.
Sighinolfi, G.P., 1969. K–Rb ratio in high grade metamorphism: a confirmation of the hypothesis of a continual crustal evolution. Contrib. Mineral. Petrol. 21, 346–356.
Simonen, A., 1953. Stratigraphy and sedimention of the Svecofennidic, early Archean supracrustal rocks in southwestern Finland. Bull. Comm. Gèol. Fin. 160, 1–64.
Smalley, P.C., Field, D., 1991. REE, Th, Hf, Ta in Bamble gabbros (Southern Norway) and their amphibolitized equivalents: implications for gabbro tectonic setting. Precambrian Res. 53, 233–242.
Smalley, P.C., Field, D., Lamb, R.C., Clough, P.W.L., 1983. Rare earth, Th–Hf–Ta and large-ion lithophile element variations in metabasites from the Proterozoic amphibolite–granulite transition zone at Arendal, south Norway. Earth Planet. Sci. Lett. 63, 446–458.
Söderlund, U., Patchett, P.J., Vervoort, J.D., Isachsen, C.E., 2004. The ^{176}Lu decay constant determined by Lu–Hf and U–Pb isotope systematics of Precambrian mafic intrusions. Earth Planet. Sci. Lett. 219, 311–324.
Steiger, R.H., Jäger, E., 1977. Subcommission on geochronology: convention on the use of decay constants in geo- and cosmochronology. Earth Planet. Sci. Lett. 36, 359–362.
Stephenson, N.C.N., 2000. Geochemistry of granulite-facies granitic rocks from Battye Glacier, northern Prince Charles Mountains, East Antarctica. Aust. J. Earth Sci. 47, 83–94.
Sun, S.S., McDonough, W.F., 1989. Chemical and isotopic systematics of oceanic basalts: implications for mantle composition and processes. Geol. Soc. Lond. Spec. Publ. 42, 313–345.
Sun, M., Zhang, L.F., Wu, J.H., 1996. The origin of the Early Proterozoic Kuandian Complex: evidence from geochemistry. Acta Geol. Sin. 70, 207–222 (in Chinese with English abstract).
Takanashi, K., Shuto, K., Sato, M., 2011. Origin of Late Paleogene to Neogene basalts and associated coeval felsic volcanic rocks in Southwest Hokkaido, northern NE Japan arc: constraints from Sr and Nd isotopes and major- and trace-element chemistry. Lithos 125, 368–392.
Taylor, S.R., McLennan, S.H., 1985. The Continental Rust: Its composition and Evolution. Blackwell, Oxford (312 pp.).
Taylor, S.R., Rudnick, R.L., McLennan, S.M., Eriksson, K.A., 1986. Rare element patterns in Archean high-grade metasediments and their tectonic significance. Geochim. Cosmochim. Acta 50, 2267–2279.
Trendall, A.F., 2002. The significance of iron-formation in the Precambrian stratigraphic record. Spec. Publ. Int. Assoc. Sedimentol. 33, 33–66.
Wan, Y.S., Song, B., Liu, D.Y., Wilde, S.A., Wu, J.S., Shi, Y.R., Yin, X.Y., Zhou, H.Y., 2006. SHRIMP U–Pb zircon geochronology of Paleoproterozoic metasedimentary rocks in the North China Craton: evidence for a major Late Paleoproterozoic tectonothermal event. Precambrian Res. 149, 249–271.
Wan, Y.S., Dong, C.Y., Xie, H.Q., Wang, S.J., Song, M.C., Xu, Z.Y., Wang, S.Y., Zhou, H.Y., Ma, M.Z., Liu, D.Y., 2012. Formation ages of the early Precambrian BIFs in the North China Craton: SHRIMP zircon U–Pb dating. Acta Geol. Sin. 86, 1447–1478 (in Chinese with English abstract).
Wang, S.T., Gao, M.X., Wan, Z.J., Sun, S.L., 2007. Geological characteristics of Paleoproterozoic metamorphic sedimentary iron deposit in east part of Changyi area in Shandong Province. Shandong Land Res. 23, 45–48 (in Chinese with English abstract).
Wang, S.J., Wan, Y.S., Zhang, C.J., Yang, E.X., Song, Z.Y., Wang, L.F., Wang, J.G., 2009. Forming ages of early Precambrian metamorphic strata in Shandong Province—proofs of zircon SHRIMP U–Pb dating. Shandong Land Resour. 25, 18–24 (in Chinese with English abstract).
Wang, F., Liu, F.L., Liu, P.H., Liu, J.H., 2010. Metamorphic evolution of Early Precambrian khondalite series in North Shandong Province. Acta Petrol. Sin. 26, 2057–2072 (in Chinese with English abstract).
Winchester, J.A., Floyd, P.A., 1976. Geochemical magma type discrimination: application to altered and metamorphosed basic igneous rocks. Earth Planet. Sci. Lett. 28, 459–469.
Winkler, H.G.F., 1976. Petrogenesis of Metamorphic Rocks, 4th edition. Springer-Verlag, Berlin (320 pp.).
Woodhead, J., Hergt, J., Shelley, M., Eggins, S., Kemp, R., 2004. Zircon Hf-isotope analysis with an excimer laser, depth profiling, ablation of complex geometries and concomitant age estimation. Chem. Geol. 209, 121–135.
Wronkiewicz, D.J., Condie, K.C., 1987. Geochemistry of Archean shales from the Witwatersrand Supergroup, South Africa: source-area weathering and provenance. Geochim. Cosmochim. Acta 51, 2401–2416.
Xia, L.Q., Xu, X.Y., Xia, Z.C., Li, X.M., Ma, Z.P., Wang, L.S., 2004. Petrogenesis of Carboniferous rift_related volcanic rocks in the Tianshan, northwestern China. Geol. Soc. Am. Bull. 116, 419–433.
Xia, L.Q., Xia, Z.C., Xu, X.Y., Li, X.M., Ma, Z.P., 2007. The discrimination between continental basalt and island arc basalt based on geochemical method. Acta Petrol. Mineral. 26, 77–89 (in Chinese with English abstract).
Xie, L.W., Zhang, Y.B., Sun, J.F., Wu, F.Y., 2008. In situ simultaneous determination of trace elements, U–Pb and Lu–Hf isotopes in zircon and baddeleyite. Chin. Sci. Bull. 53, 1565–1573.
Xu, H.Y., Dong, Y.F., Xu, W.X., Tian, X.L., Zhang, D.M., 2011. Geological characteristics and ore prospecting direction of iron deposits in Laizhou-Anqiu area in Shandong Province. Shandong Land Resour. 27, 9–13 (in Chinese with English abstract).
Yang, K.F., Fan, H.R., Santosh, M., Hu, F.F., Wilde, S.A., Lan, T.G., Lu, L.N., Liu, Y.S., 2012. Reactivation of the Archean lower crust: implications for zircon geochronology, elemental and Sr–Nd–Hf isotopic geochemistry of late Mesozoic granitoids from northwestern Jiaodong Terrane, the North China Craton. Lithos 146–147, 112–127.
Yu, Z.C., 1996. New progress of research on the Fenzishan Group in the Pingdu-Laizhou area in the west of Jiaobei region. Shandong Geol. 12, 24–34 (in Chinese with English abstract).
Zhai, M.G., 2010. Tectonic evolution and metallogenesis of North China Craton. Mineral Deposits 29, 24–36 (in Chinese with English abstract).
Zhai, M.G., Peng, P., 2007. Paleoproterozoic events in the North China Craton. Acta Petrol. Sin. 23, 2665–2682 (in Chinese with English abstract).
Zhai, M.G., Santosh, M., 2011. The Early Precambrian odyssey of the North China Craton: a synoptic overview. Gondwana Res. 20, 6–25.
Zhai, A.M., Shen, B.F., 1994. Proterozoic tectonic evolution and metallogeny in China. In: Zhang, Y.X., Liu, L.D. (Eds.), Precambrian Ore-deposits and Tectonics. Seismological Press, Beijing, pp. 125–146 (in Chinese).
Zhang, Q.S., 1988. Early Proterozoic crustal evolution in Liaodong peninsula. In: Mao, C.Y., Liu, L.D. (Eds.), Selected Papers of Zhang Qiusheng. Jilin Science and Technology Press, Jilin, pp. 45–51 (in Chinese).
Zhang, J., Nozaki, Y., 1996. Rare earth elements and yttrium in seawater: ICP-MS determinations in the East Caroline, Coral Sea, and South Fiji basins of the western South Pacific Ocean. Geochim. Cosmochim. Acta 60, 4631–4644.
Zhang, Q.S., Yang, Z.S., 1988. Early Crust and Mineral Deposits of Liaodong Peninsula, China. Geological Publishing House, Beijing 218–450 (in Chinese with English abstract).
Zhang, H.F., Yin, J.F., Tang, Y.J., Li, X.H., Feng, C., Santosh, M., 2011a. Phanerozoic reactivation of the Archean North China Craton through episodic magmatism: evidence from zircon U–Pb geochronology and Hf isotopes from the Liaodong Peninsula. Gondwana Res. 19, 446–459.
Zhang, X.J., Zhang, L.C., Xiang, P., Wan, B., Pirajno, F., 2011b. Zircon U–Pb age, Hf isotopes and geochemistry of Shuichang Algoma-type banded iron-formation, North China Craton: constraints on the ore-forming age and tectonic setting. Gondwana Res. 20, 137–148.

Zhang, L.C., Zhai, M.G., Wan, Y.S., Guo, J.H., Dai, Y.P., Wang, C.L., Liu, L., 2012a. Study of the BIF-iron deposits in the North China Craton: progresses and questions. Acta Petrol. Sin. 28, 3431–3445 (in Chinese with English abstract).

Zhang, L.C., Zhai, M.G., Zhang, X.J., Xiang, P., Dai, Y.P., Wang, C.L., Pirajno, F., 2012b. Formation age and tectonic setting of the Shirengou Neoarchean banded iron deposit in eastern Hebei Province: constraints from geochemistry and SIMS zircon U–Pb dating. Precambrian Res. 222–223, 325–338.

Zhao, G.C., Wilde, S.A., Cawood, P.A., Sun, M., 2001. Archean blocks and their boundaries in the North China Craton: lithological, geochemical, structural and P–T path constraints and tectonic evolution. Precambrian Res. 107, 45–73.

Zhao, G.C., Sun, M., Wilde, S.A., Li, S.Z., 2005. Late Archean to Paleoproterozoic evolution of the North China Craton: key issues revisited. Precambrian Res. 136, 177–202.

Zhao, G., Cawood, P.A., Li, S., Wilde, S.A., Sun, M., Zhang, J., He, Y., Yin, C., 2012. Amalgamation of the North China Craton: key issues and discussion. Precambrian Res. 222–223, 55–76.

Zheng, Y.F., Xiao, W.J., Zhao, G.C., 2012. Introduction to tectonics of China. Gondwana Res. 23, 1189–1206.

Zhou, X.W., Wei, C.J., Geng, Y.S., 2007. Phase equilibria and P–T path of high- and low-pressure pelitic granulites from the Jiaobei massif. Earth Sci. Front. 14, 135–143 (in Chinese with English abstract).